B. Nold

Comparison of Dimensionally Similar Turbulence in TJ-K and ASDEX-Upgrade

Universität Stuttgart

Institut für Plasmaforschung

Max-Planck-Institut für Plasmaphysik

Comparison of Dimensionally Similar Turbulence in TJ-K and ASDEX Upgrade

Diplomarbeit

Bernhard Nold

Zusammenfassung

Alternative Energiequellen werden aufgrund von fortschreitendem Klimawandel und weltweit steigendem Energiebedarf immer wichtiger. Die kontrollierte Kernfusion wird möglicherweise in der zweiten Hälfte dieses Jahrhunderts einen Beitrag zur Energieversorgung liefern. Vor der Nutzung dieser Technologie müssen aber noch viele grundlegende physikalische Prozesse untersucht werden. Im Rahmen dieser Arbeit wurden Turbulenz Studien in dimensional ähnlichen Plasmaentladungen angestellt. Das Verständnis turbulenter Transportprozesse ist wichtig für die Effizienz zukünftiger Fusionsanlagen. Der turbulente Transport führt zum Verlust von Energie und Teilchen aus dem Plasma. Die Energie geht dem Plasma verloren und wird an die Wand abgegeben.

Mit Hilfe von Langmuir-Sonden wurden Fluktuationen im Niedertemperaturplasma des Torsatrons TJ-K mit denen in der Randschicht des heißen Fusionsplasmas im Tokamak ASDEX Upgrade verglichen. Das Torsatron TJ-K befindet sich am Institut für Plasmaforschung in Stuttgart, während der Tokamak ASDEX Upgrade (AUG) am Max-Planck-Institut für Plasmaphysik in Garching betrieben wird. Für beide Maschinen wurden poloidale Langmuir-Sondenarrays aufgebaut und zum Einsatz gebracht. In TJ-K wurde in räumlich begrenzten Wasserstoff- und Heliumentladungen gearbeitet. In AUG wurden Ohmsche, das bedeutet induktiv geheizte, Deuteriumentladungen untersucht. Gleichgewichtsprofile und Fluktuationen von Dichte und Potential konnten experimentell an beiden Maschinen sowohl in der Abschälschicht, als auch im Einschlussbereich des Plasmas gemessen werden. Zur Datenanalyse wurden verschiedene Verfahren eingesetzt, deren Ergebnisse im Bezug zu theoretischen Modellen und ähnlichen Experimenten diskutiert werden.

In beiden Experimenten wurden die Dichteabfalllängen bestimmt und damit berechnete dimensionslose Parameter verglichen. Die Auswertung dieser Ergebnisse haben die dimensionale Ähnlichkeit von TJ-K und der Randschicht von ASDEX Upgrade bestätigt.

Die Untersuchung der poloidalen Phasengeschwindigkeit der turbulenten Strukturen mittels Kreuzkorrelationsanalysen offenbarte einen abrupten Richtungswechsel der Phasengeschwindigkeit im Bereich der letzten geschlossenen Flussfläche. Im Einschlussbereich bewegt sich die Phase der Fluktuationen in Richtung der elektronendiamagnetischen Driftrichtung. In Abwesenheit poloidaler Hintergrundströmungen erwartet man dies für

von Driftwellen getriebene Turbulenz, wie sie in TJ-K nachgewiesen wurde. In AUG deuten die gemessenen Floatingpotentialprofile auf radiale elektrische Felder hin, wie sie auch von der Doppler-Reflektometrie besttigt wurden. Diese Felder bewirken poloidale $E \times B$-Driften und führen daher zu einer poloidalen Scherströmung im Hintergrundfluß. Der abrupte Richtungswechsel wird wohl eher durch diese Scherströmung hervorgerufen, als durch eine Änderung der die Turbulenz treibenden Mechanismen. Andernfalls würde man einen kontinuierlichen Übergang erwarten. Auch die Kreuzphase zwischen Dichte und poloidalen Feldfluktuationen deutet in der gesamten Randschicht von AUG auf Driftwellenturbulenz hin. In TJ-K sind Driftwellen für die beobachtete Phasengeschwindigkeit im Einschlussbereich verantwortlich, da hier im Gegensatz zu AUG kein radiales elektrisches Feld beobachtet wird.

Die poloidale Korrelationslänge verdoppelt sich im Einschlussbereich kurz vor der Separatrix. Dieses Anwachsen nahe der Scherströmung beschränkt sich mglicherweise auf die poloidale Korrelationslänge. In radialer Richtung wird Dekorrelation erwartet und damit kürzere Korrelationslängen. Die Beobachtung wäre damit ein Hinweis auf stark elongierte Strukturen. Die beobachteten Autokorrelationszeiten entsprechen dem, was man aufgrund von Phasengeschwindigkeit und Strukturgröße erwartet.

Weiterhin wurden in AUG nahe der Separatrix Hinweise auf netto Inwärtstransport beobachtet. Diese Beobachtung sollte allerdings noch durch weitere Untersuchungen überprüft werden.

Die Amplituden der relativen Dichtefluktuationen ist in beiden Experimenten vergleichbar. Die relative Standardabweichung nimmt mit dem Radius zu. Dies wird möglicherweise durch nach außen laufende Dichtestrukturen hervorgerufen, deren relative Signifikanz mit abfallender Hintergrunddichte zunimmt.

Die Wahrscheinlichkeitsdichtefunktion (PDF) ist in der Abschählschicht von TJ-K und AUG asymmetrisch und zugespitzt. Dieses wiederholte Auftreten stark erhöhter Dichteereignisse wurde bereits in verschiedenen magnetisch eingeschlossenen Plasmen beobachtet. Man spricht hierbei von Intermittenz. Nahe der Separatrix nimmt die PDF die Form einer Gaußverteilung an. Die positiven Dichteereignisse scheinen also an der Separatrix zu entstehen. Im Einschlussbereich von TJ-K wurden negative Skewness-Werte beobachtet, die auf nach innen laufende "Dichtelöcher" hindeuten könnten. Dieser Effekt wurde auch schon an anderen Maschinen beobachtet. Im Einschlussbereich von AUG wurden sowohl negative, als auch positive Werte der Skewness beobachtet, sodass hier noch keine abschließende Bewertung der Asymmetrie möglich war.

Contents

Chapter 1

Introduction

World population and its need of energy are increasing with unprecedented speed. In addition to all the employed efforts of energy saving, mankind has to look for a mixture of sustainable energy sources to satisfy future needs. Energy from nuclear fusion may play an important role in this field. It avoids climate changing CO_2 emissions, minimizes problems of nuclear waste disposal and averts dangers of proliferation and nuclear accidents. Recently the leading industrial countries expressed their interest in the field of nuclear fusion energy. One of the big challenges is the joint venture ITER, an experimental reactor that will be built in Cadarache, France.

1.1 Fusion Energy

In a future fusion power plant, deuterium D and tritium T will transform into helium He and a neutron. The released binding energy in such reactions is 17.6 MeV [1]. 1 g of a D-T mixture could liberate a total energy of 2×10^{30} eV. This corresponds to more than 4 times the energy that could theoretically be won out of 1 g pure uranium U-235 by nuclear fission reactions. To free the same amount of energy, almost 8000 liters of oil have to be burned.

Nuclear fusion reactions occur when D and T clash together with high kinetic energies. At high temperatures of about 100 million degree Kelvin, a optimum of the reaction probability is reached [1]. At these temperatures, nuclei and electrons are no longer bound together. The ionized gas is called plasma. An example for a fusion plasma in everyday live is the sun. On earth, there are two distinct approaches to utilize fusion energy: Inertial fusion and magnetic confinement. In the first approach small fuel pellets are compressed by laser radiation. This leads to a micro explosion, which is not only interesting for energy production but also for military purposes. The present work is linked to the magnetic confinement approach. Its concepts are introduced in the next section.
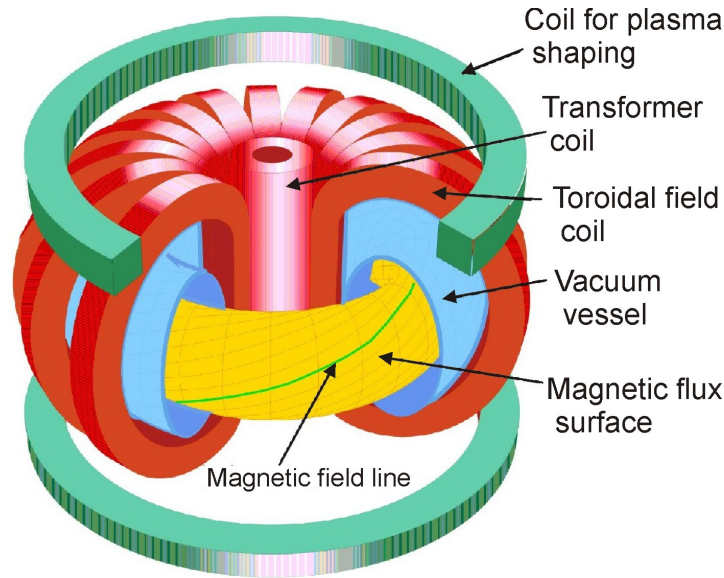
Figure 1.1: Schematic drawing of a tokamak.

1.2 Magnetic confinement

Plasmas are cooled down and neutralized, if they are in contact with solid surfaces. Heavy atoms from the wall dilute the plasma and cool it down by radiation. Plasmas are confined in magnetic fields, to minimize its contact with walls and to maintain a low level of impurities. The trajectory of a charged particle is bend in a magnetic field due to the Lorentz force. In a homogeneous magnetic field, the particle gyrates around a guiding center. The particle motion along this guiding center, i.e. parallel to the magnetic field, is free. Different magnetic configurations have been tested and finally toroidally closed field lines were found to be the best solution. Two different toroidal concepts have been developed: The tokamak Fig. 1.1 and the stellarator Fig. 1.2. The toroidal magnetic field is not homogeneous, it decays from the inner to the outer wall of the torus. In a pure toroidal magnetic field, this leads to a vertical charge separation of ions and electrons in the torus. The resulting vertical electric field causes an $E \times B$ drift, that moves the plasma to the outer wall. Therefore, an additional magnetic field is generated poloidally to compensate the charge separation. The superposition of toroidal and poloidal magnetic field is a helical one where the field lines are found in closed flux surfaces. This configuration is able to confine the plasma.

Fig. 1.1 shows the sketch of a tokamak. The toroidal magnetic field is generated by planar coils. The poloidal field component arises due to a toroidal plasma current, which is induced from the transformer coils in the center of the torus. Additional horizontal coils are used for plasma shaping and stabilization. A magnetic field line and its corresponding flux surface are represented in the figure. The experiment ASDEX Upgrade, introduced in section 3.2, is a tokamak.
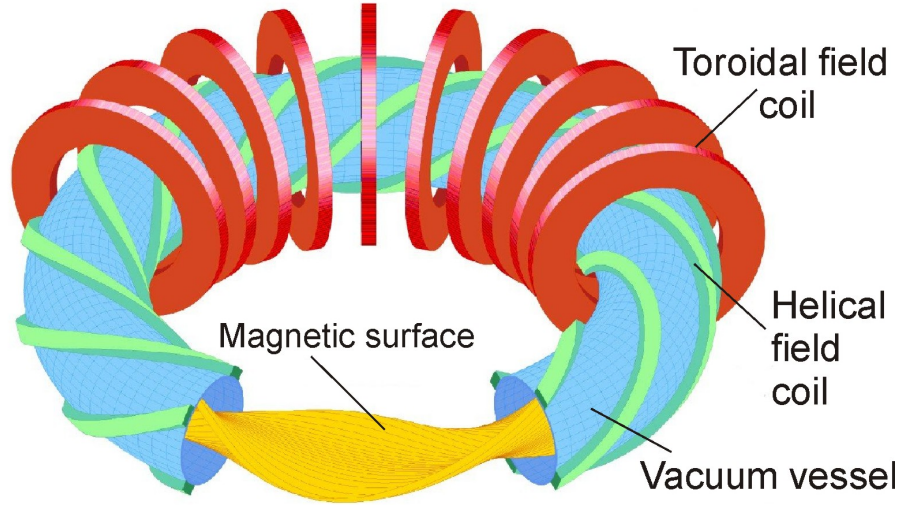
Figure 1.2: Schematic drawing of a stellarator.

Several configurations have been proposed to generate toroidal and poloidal fields with external field coils only. Such devices are called stellarators. In contrast to tokamaks, the plasma shape of stellarators is toroidally not symmetric. They can operate in steady state because their confinement does not depend on an induced plasma current. Fig. 1.2 shows the toroidal and helical field coils of a stellarator. Section 3.1 presents the torsatron TJ-K. This is a special type of stellarator, where no toroidal field coils are necessary.

1.3 Ignition

To serve as an energy producing system, the plasma has to be ignited. In an ignited plasma all energy losses are compensated by the α particles of the fusion reaction.

$$^3H \; + \; ^2H \; = \; T \; + \; D \; \rightarrow \; ^4He \, (3.52 \, \mathrm{MeV}) \; + \; n \, (14.06 \, \mathrm{MeV}) \tag{1.1}$$
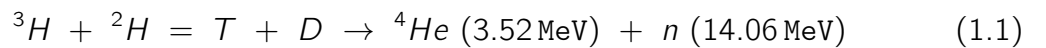
The energy of the α particles is $3.52 \, \mathrm{MeV}$. The rest of the fusion energy is transported out of the plasma by the neutrons, which cannot be confined by the magnetic field and do not interact with the plasma. The plasma energy is lost by radiation and transport processes. The condition of ignition is given by the triple product and may be approximated according to [1]

$$\bar{n} \, \bar{T} \, \tau_E > 3 \times 10^{24} \, \mathrm{eV \, s \, m^{-3}}, \tag{1.2}$$

if the bremsstrahlung is neglected. With typical mean densities $\bar{n} \approx 2 \times 10^{+20} \, \mathrm{m^{-3}}$ and temperatures $\bar{T} \approx 15 \, \mathrm{keV}$, an energy confinement time of $\tau_E \approx 3 \, \mathrm{s}$ would be necessary for ignition. Such high energy confinement times were not yet achieved because too much energy is lost by transport processes perpendicular to the magnetic field.

1.4 Scope of this Work

A key issue for the understanding of cross field transport in magnetically confined plasmas is plasma turbulence. In this work, plasma turbulence is investigated at the transition region from closed to so-called open magnetic field lines. For this purpose, the dimensionally similar plasmas of the torsatron TJ-K and the tokamak ASDEX Upgrade are compared by means of Langmuir probe measurements. Plasma equilibria and statistical properties are investigated to learn about the driving mechanisms of turbulent transport. Coherent structures within the fluctuation data, which are supposed to substantially contribute to the turbulent losses, are explored by correlation analyses. Experiments are carried out on TJ-K and AUG to study how the dimensional similarity reflects in the statistic of the turbulent fluctuations.

Chapter 2 presents the theoretical background of plasma turbulence. Descriptions of the experiments TJ-K and ASDEX Upgrade are found in chapter 3. The same chapter introduces the theory of Langmuir probes and the probe arrays designed for this work. Chapter 4 is dedicated to the concept of dimensional similarity. The employed data analyses are presented chapter 5. The experimental results of TJ-K and ASDEX Upgrade are given in chapters 6 and 7, respectively. A short summary is given together with conclusions from both devices in chapter 8.

Chapter 2
Plasma Turbulence

The energy confinement time τ_E has to be sufficiently long, to achieve ignition of a fusion plasma. The link between τ_E and diffusion is shown in section 2.1. Section 2.2 introduces two approaches to diffusion in the plasma. This model is extended in section 2.3 to a second dimension and with independent potential and density fluctuations. The relation between these fluctuations is imposed by a dominant plasma instability. Interchange and drift-wave instabilities are supposed to drive turbulence and turbulent transport in the plasma edge and scrape-off layer (SOL). These instabilities are introduced in sections 2.4 and 2.5, respectively. The understanding of these mechanisms is a route to prediction and optimization of energy confinement time and plasma wall interaction in future power plants.

2.1 Energy Confinement

The global energy confinement time τ_E is related to the minor plasma radius a and the heat diffusivity χ according to [2]

$$\tau_E \approx f \frac{a^2}{\chi},\qquad(2.1)$$

where f depends on the profile shape. τ_E increases with larger minor radii, improved plasma shape and lower heat diffusivity. Increasing a is the simplest way to achieve higher confinement times, but it is also the most expensive one. The influence of the plasma shape on the confinement is investigated in several devices, e.g. TCV in Lausanne [3, 4] and DIII-D in San Diego [5]. Of special interest is the diffusivity, which is governed by the underlying physics of turbulent transport. The physics is not yet fully understood. Model predictions of global confinement times based on small scale fluctuations are subject of active research. Alternatively, the confinement is investigated by empirical scaling laws, which allow to extrapolate confinement times to larger fusion devices (see e.g. Ref. [2]). For studies using dimensionally similar discharges (see chapter 4), the diffusivity is

expressed in terms of the Bohm diffusion coefficient $D_B = \rho_s c_s$ and a function F:

$$\chi = D_B F(\rho_*, \nu_*, \beta_*, \ldots) \tag{2.2}$$

F depends on non-dimensional parameters like the normalized versions of drift-scale $\rho_* = \rho_s/a$, collisionallity ν_* and plasma-beta β_*. ν_* and β_* are crucial control parameters of the plasma dynamics similar to the Reynolds number in neutral fluid dynamics. They will be introduced in more detail in section 4.1. ρ_* is the drift-scale $\rho_s = c_s/\omega_{ci}$ normalized to the minor plasma radius a. $c_s = \sqrt{(\gamma_e Z T_e + \gamma_i T_i)/m_i}$ is the ion sound velocity and $\omega_{ci} = eB/m_i$ the ion gyrofrequency. The equations are valid for ions of charge number Z, mass m_i, temperature T_i and an adiabatic coefficient γ_i. The electrons have the temperature T_e and the adiabatic coefficient $gamma_e$. B denotes the magnetic field strength and e the elementary charge. For nuclear fusion, the parameters ν_* and β_* are already achieved. ρ_*, however, will be much smaller in future devices, due to the high magnetic field strength. Scaling studies focus on the variation of ρ_* holding ν_*, β^*, etc. fixed in dimensionally similar discharges [6, 7]. Moreover, ρ_s plays the role of a scaling parameter for characteristic spatial scales in micro turbulence. For drift-wave turbulence, $L_c \sim \rho_s$ is expected from theory [8], where L_c is the correlation length of turbulent structures. In TJ-K discharges, which are dominated by drift-wave turbulence [9, 10, 11], a scaling law according to $L_c \sim \sqrt{\rho_s}$ was found experimentally [12, 13].

2.2 Microscopic Turbulence

In this section, the dependence of the diffusion coefficient on plasma-potential fluctuations is deduced from two different models. At first, a few basic considerations are presented. Fig. 2.1 shows a monotonic density gradient from a magnetically confined plasma. A homogeneous magnetic field **B** points perpendicular out of the surface. Potential perturbations outside the represented area create a homogeneous electric field **E** from the bottom to the top. In this situation, the **E** × **B** drift

$$v_{E \times B} = \frac{\mathbf{E} \times \mathbf{B}}{B^2} \tag{2.3}$$

acts on all particles in the considered area. All particles in this area are displaced to the right side, i.e. radially outward, with the drift velocity $v_{E \times B}$. In a turbulent plasma, potential perturbations are temporally and spatially unstable. For this first approach, only a small area in the plasma is considered. It is assumed that only the absolute value of the poloidal electric field $\tilde{E}_\theta = \tilde{\phi}_{bottom} - \tilde{\phi}_{top}$ fluctuates. If E_θ persists for a time τ_c, the radial drift of the particles $v_{E_\theta \times B}$ leads to a radial displacement

$$\delta r \sim v_{E_\theta \times B} \tau_c. \tag{2.4}$$

Figure 2.1: Radial $E \times B$ drift velocity in a magnetized plasma. The poloidal electric field is caused by plasma-potential perturbations at the top and bottom of the considered plasma volume.
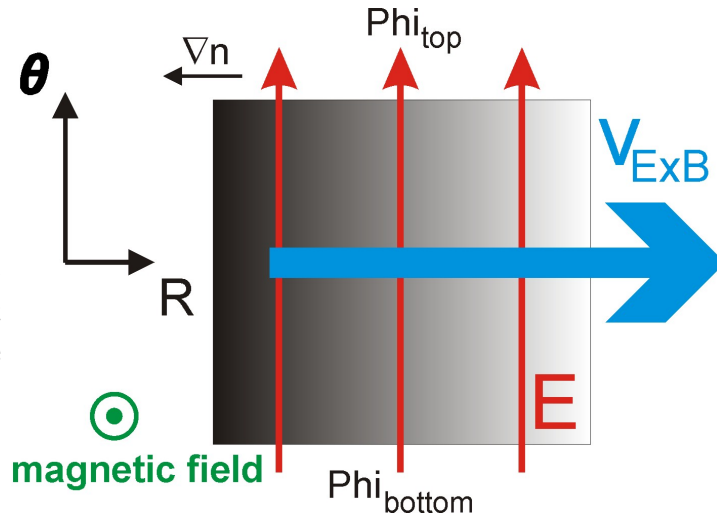
τ_c is the correlation time of the fluctuation, i.e. the time during which the potential perturbations persist.

In a random walk model, the diffusion coefficient is $D = L^2/(2t)$, for the characteristic length L and time t. These characteristic scales can be replaced by the characteristic quantities of the fluctuations from equation 2.4. This leads to the first approximation of the diffusion coefficient in a turbulent plasma based on microscopic quantities:

$$D \approx \frac{\delta r^2}{2\tau_c} \sim \frac{v_{E_\theta \times B}^2}{2}\tau_c \tag{2.5}$$

The second approach is based on the influence of a local potential perturbation on the density gradient $\nabla n = n_{00}/a$. n_{00} is the core density and a the minor radius of the plasma. Fig. 2.2 illustrates this idealized situation, known as mixing length model.

A spatially localized potential perturbation provokes an electric field. This field drives a circular $v_{E_\theta \times B}$ drift around the initial perturbation. The drift displaces particles outward
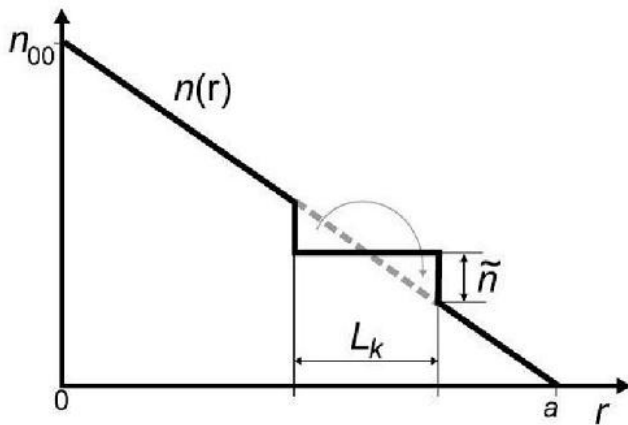

Figure 2.2: The mixing length model. A local potential perturbation provokes a circular $E \times B$ drift, that depletes the density gradient and generates the density fluctuation $\tilde{n}$ [1].

over a length L_k. This length is proportional to the displacement found in equation 2.4: $L_k \sim \delta r$. The displacement leads to a density perturbation $\tilde{n}$, which is compensated within a certain time by the background density gradient. $\tilde{n}$ is only observed, if the displacement due to the electric field occurs faster than the relaxation of the background. In this simple model, it satisfies the relation

$$\frac{2\tilde{n}}{L_k} \approx -\nabla n. \tag{2.6}$$

This relation of $\tilde{n}$ can be used for the approximation of the turbulent transport $\Gamma = \tilde{v}_{E_\theta \times B} \tilde{n}$. With equation 2.4, Γ can be expressed as

$$\Gamma \approx -\tilde{v}_{E_\theta \times B} \frac{L_k}{2} \nabla n \approx -\tilde{v}_{E_\theta \times B} \frac{\delta r}{2} \nabla n \approx -\frac{\tilde{v}_{E_\theta \times B}^2}{2} \tau_c \nabla n \approx -D \nabla n. \tag{2.7}$$

The same diffusion coefficient D is found as earlier in equation 2.5.

The correlation time τ_c is determined by the process which limits most rapidly the displacement due to the $E \times B$ drift. This may be a fast time variation of the fluctuation, the time for a particle to move along a parallel wavelength of the fluctuations or the time for collisions to displace the particles [14].

This section gave an approach to the local diffusion coefficient caused by fluctuating electric fields. For a global understanding of diffusion and transport, density fluctuations need to be taken into account and the model has to be extended to all present wavelength. The first one of these ameliorations is introduced in the next section.

2.3 Turbulent Transport

This section introduces the idea of turbulent transport processes due to plasma fluctuations. Fig. 2.3 (left side) shows the potential fluctuation $\tilde{\phi}$ in a constant density gradient. The positive potential $\tilde{\phi}$ is accompanied by a perturbation in the electric field $\tilde{E}$. In presence of the background magnetic field B, this leads to a circular $\tilde{E} \times B$ drift. This drift causes a local plasma displacement around the potential perturbation. The localized impact of poloidal electric fields was discussed in the previous section. Now the whole vortex is considered. The same amount of density is displaced radially in (top) and outward (bottom). Integration of the transport over the vertical coordinate gives a net radial transport of zero. This situation may change, if the potential perturbation is accompanied by a density perturbation. In the middle of Fig. 2.3 a positive density perturbation at the bottom of the vortex is indicated as a black shadow. More density is displaced outward at the bottom of the vortex than inward on the top. Integration of the transport now gives a positive outward directed flux. On the right side of the figure, density and potential perturbation are in phase. In this case again, no net transport is
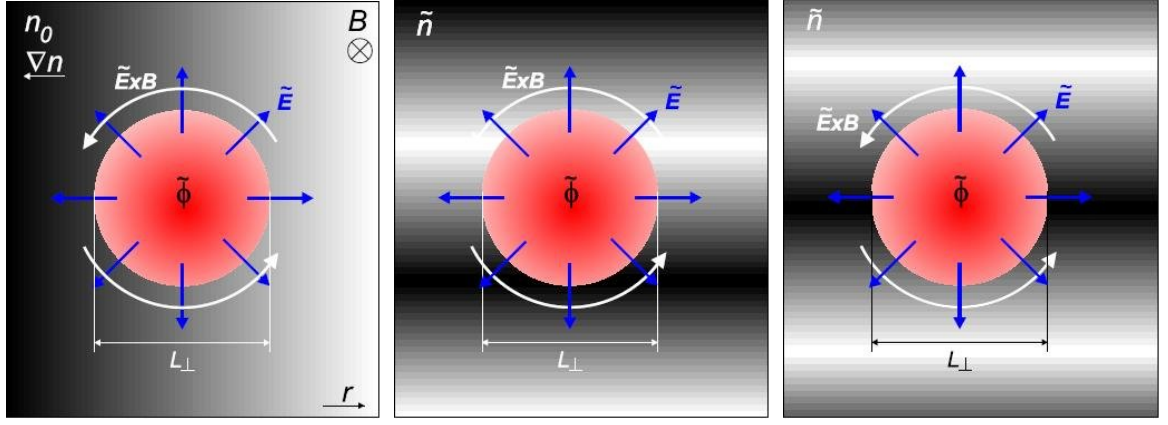
Figure 2.3: Mechanism of radial transport due to electrostatic turbulence. Potential fluctuation in unperturbed density gradient (left) and with additional density fluctuations out of phase (middle) and in phase (right) [13].

observed because the same amount of density is displaced on top and bottom of the vortex. On the other hand, a phase shift of $-\pi/2$ between density and potential fluctuation could lead to net inward transport.

The turbulent transport $\tilde{\Gamma}$ averaged over a flux surface F is given by

$$\tilde{\Gamma}(t) = \langle \tilde{v}_{E_\theta \times B}(t)\tilde{n}(t)\rangle_F = \frac{1}{B}\langle \tilde{E}_\theta(t)\tilde{n}(t)\rangle_F. \tag{2.8}$$

In most experiments, the fluctuations on an entire flux surface are not accessible. For this reason, the local mean transport is usually investigated at a single point in space. The necessary data, $\tilde{E}_\theta(t)$ and $\tilde{n}(t)$, can be measured with three slightly poloidally separated Langmuir probes. In this case, the average over the whole flux surface in equation 2.8 is replaced by a temporal average. The local mean transport is then obtained by [15]

$$\Gamma = \langle \tilde{E}_\theta(t)\tilde{n}(t)\rangle_t = \int d\omega |\hat{E}_\theta^*(\omega)||\hat{n}(\omega)|\cos(\varphi(\omega)), \tag{2.9}$$

where $\varphi(\omega) = \varphi_n(\omega) - \varphi_E(\omega)$ is the cross-phase between density and electric field fluctuations at frequency ω. The coefficients of the Fourier transforms of the fluctuating quantities $\tilde{f}(t)$ are denoted by $\hat{f}(\omega)$ and their complex conjugate with the asterisk. Equation 2.9 shows that the sign of the radial transport is determined by the cross-phase. This is consistent with the qualitative considerations illustrated in Fig. 2.3. For $\varphi(\omega) = \pi/2$, no radial transport occurs. Outward (inward) transport is observed for cross-phases $\varphi(\omega) < \pi/2$ ($\varphi(\omega) > \pi/2$).

In this section, it has been shown how density and potential perturbations cause turbulent transport. The following two sections present the plasma instabilities, which are supposed to drive turbulence in the edge mainly.
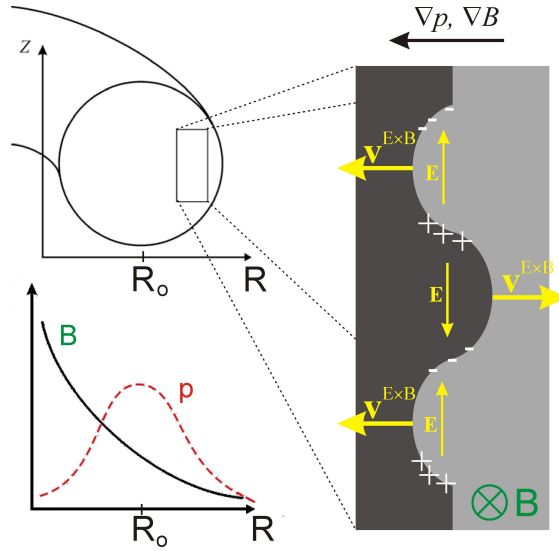
Figure 2.4: Model of the interchange instability [16].

2.4 Interchange Instability

The interchange instability is characterized by the interchange of plasma in a density gradient. The driving mechanism for the development of an interchange instability is based on curvature v^c and gradient drift $v^{\nabla B}$. These drifts are given by

$$\mathbf{v}^c = 2W_{||}\frac{\mathbf{R}_C \times \mathbf{B}}{qR_C^2B^2} \tag{2.10}$$

and

$$\mathbf{v}^{\nabla B} = -W_{\perp}\frac{\nabla_{\perp}B \times \mathbf{B}}{qB^3}. \tag{2.11}$$

They depend on the particle energies parallel ($W_{||}$) and perpendicular ($W_{\perp}$) to the magnetic field. $\mathbf{R}_C$ is the curvature radius of the magnetic field $\mathbf{B}$. In both cases, the drift direction is sensitive to the particle charge q and therefore causes charge separation. Fig. 2.4 shows on the left side a part of a toroidally confined plasma (top) and the corresponding profiles of plasma pressure p and toroidal magnetic field strength (bottom). The mechanism of interchange instabilities is explained in the window on the right-hand side. It is a zoom into the pressure gradient at the low-field side of the confined plasma. Inside the window, the magnetic field and the pressure increase from the right to the left. The magnetic field points perpendicular into the figure. An initial perturbation of the density gradient is observed between high (dark) and low (light) pressure areas. According to equations 2.10 and 2.11, gradient and curvature drift lead to a charge separation in this sinusoidal density perturbation. As a consequence, positive charges are accumulated at the top and negative at the bottom of the high pressure perturbation. The space charges cause poloidal electric fields, indicated as vertical arrows in the figure. The resulting radial $E \times B$ drift amplifies the initial perturbation. The high density
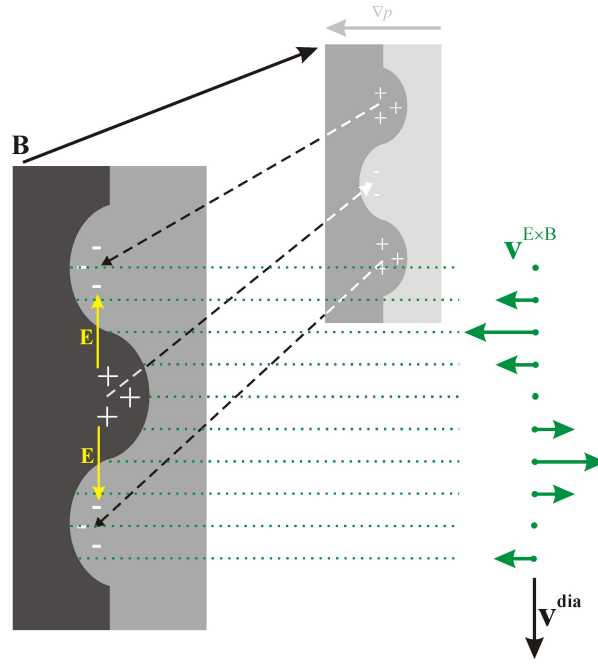
Figure 2.5: Model of the drift wave instability [16].

perturbations are moved radially further outward, while the low density perturbations are shifted inward. The cross-phase between density and poloidal electric field is $\varphi = \pi$. This corresponds to the maximum of outward directed transport, as discussed in the previous section. This amplification of the initial perturbations is only found on the low-field side. For $R < R_0$, the pressure and magnetic field gradients are opposed. In this case, the $E \times B$ drift reduces an initial perturbation and stabilizes the plasma. The curvature at the high-field side is called favorable and the curvature at the low-field side unfavorable. Interchange instabilities do not propagate poloidally, except in presence of background flows. They are elongated along the magnetic field lines. Their parallel wave length is infinite and the parallel wave number is therefore $k_{\parallel} = 0$.

2.5 Drift Wave Instability

In contrary to the interchange instabilities discussed in the previous section, the parallel wavenumber of drift waves is $k_{\parallel} > 0$. For this reason, a two dimensional picture is not sufficient to understand the mechanism of drift waves. A drawing of the three dimensional drift wave model is shown in Fig. 2.5. Initial perturbations of the density gradient are indicated by dark and light regions in fore- and background of the figure.

Because of their low mass, electrons are supposed to react instantly on parallel density perturbations. This electron reaction is indicated by dashed arrows parallel to the magnetic field. As a result, positive space charge is observed in high density regions and

negative space charge in low density regions. This situation is indicated by $+$ and $-$ signs in the picture. Poloidal electric fields and the resulting $E \times B$ drifts are represented as vertical and horizontal arrows, respectively. The cross-phase between density and poloidal electric field is $\varphi = \pi/2$. The net radial transport is therefore zero as discussed in section 2.3. The poloidal profile of the $E \times B$ drift is shown on the right side of the figure. This leads to a downward propagation of the density perturbation. The phase velocity of drift waves is poloidally parallel to the electron diamagnetic drift, which is defined as

$$\mathbf{v}_{dia}^{e} = -\frac{\nabla p \times \mathbf{B}}{enB^2}.$$

(2.12)

The perpendicular wave number of drift waves is much larger than the parallel one $k_\perp \gg k_\parallel$.

Chapter 3

Experimental Setups

In this work, measurements were carried out with poloidal Langmuir-probe arrays in the torsatron TJ-K and the tokamak ASDEX Upgrade (AUG). This chapter introduces briefly the devices TJ-K at IPF Stuttgart (Sec. 3.1) and AUG at IPP Garching (Sec. 3.2). In section 3.3, the fundamentals of Langmuir-probe theory are presented followed by a detailed description of the probe arrays constructed for the low-temperature plasma in TJ-K (Sec. 3.4) and the hot fusion plasma in AUG (Sec. 3.5).

3.1 The Torsatron TJ-K

The torsatron TJ-K is a stellerator operated with low-temperature plasmas from 1999 to 2004 in Kiel and since 2005 at the Institut für Plasmaforschung in Stuttgart. Its major and minor plasma radii are 0.6 and 0.1 m, respectively. The magnetic field of up to 0.3 T is generated by two vertical and one helical ($l = 1$) field coil (Fig. 3.1). The latter is wound six times around the toroidal vacuum vessel. This leads to a magnetic field configuration that repeats every 60 degrees ($m = 6$). Two electron-cyclotron-resonance heating (ECRH) systems are available with operation frequencies of 2.45 and 8.25 GHz for low ($B_{axis} = 0.072$ T) and high magnetic field ($B_{axis} = 0.276$ T) operation. Ohmic losses in the field coils limit steady-state operation. At low magnetic field, this limit is reached after 45 minutes, at high magnetic field after a few minutes. Working gases are hydrogen, deuterium, helium, neon and argon. Typically, plasma densities of $n_e = 5x10^{17}$ m^{-3}, electron temperatures of $T_e = 10$ eV and ion temperatures $T_i < 1$ eV are achieved. The line integrated plasma density is permanently monitored with a microwave interferometer. Two manipulators are installed, one for 1D and the other for 2D probe positioning in the vessel. Beside these devices several fixed multi-probe arrays with up to 128 probes are available to be installed in the vessel. In the present work, only Langmuir probes have been installed, but earlier investigations also used electron emitting [17] and magnetic probes [18]. Because of good accessibility for probes and steady state operation, TJ-K is well adapted for statistical turbulence studies. The position in TJ-K is usually given
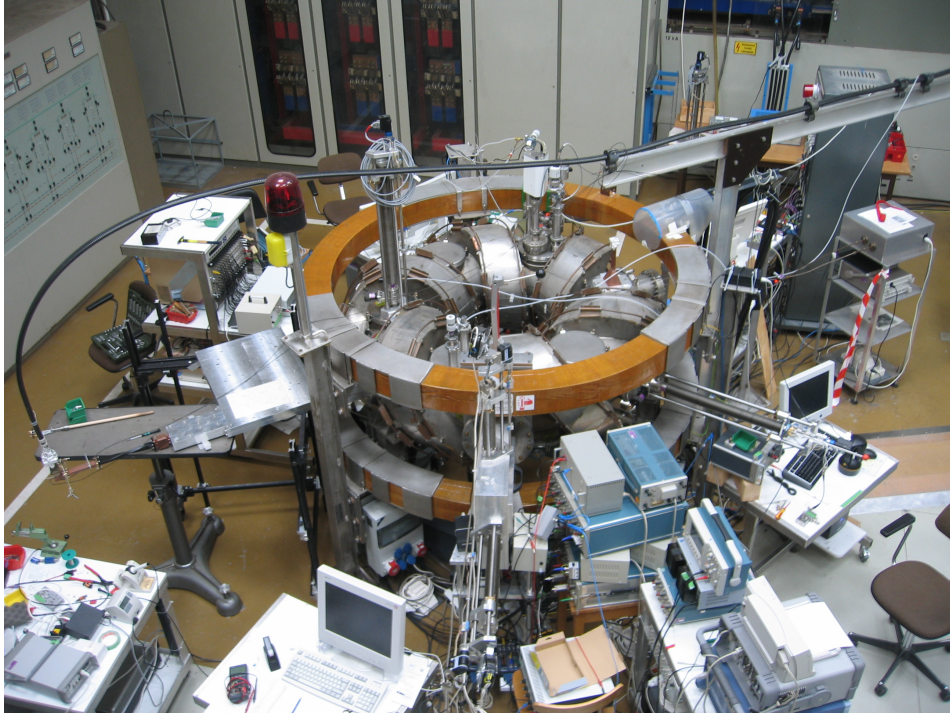
Figure 3.1: View on the torsatron TJ-K in the experimental hall at IPF Stuttgart. The two horizontal rings are the vertical magnetic field coils. The toroidal vacuum vessel and the helical field coil can be seen in-between.

in vessel coordinates $R - R_0$, with the absolute radial position R and the major radius $R_0 = 0.6\,\text{m}$. The measurements of this work were all performed through the outer ports, where the plasma center is located at $R - R_0 = +4.5\,\text{cm}$. Table 3.1 compares machine and plasma parameters of TJ-K and the tokamak ASDEX Upgrade, which is introduced in the next section. More details about TJ-K can be found in Refs. [19] and [20].

To homogenize the plasma in the scrape-off layer (SOL), a limiter plate was mounted in the vacuum vessel [16] . It covers the whole poloidal cross section of the vessel except a central hole. The shape of the hole is aligned to a magnetic flux surface in front of an outer port. This limits the confined plasma core in the range $R - R_0 = -1.2$ to $+8.8\,\text{cm}$ at $z = 0\,\text{cm}$. The position of the last closed flux surface is well defined and the scrape-off layer (SOL) is increased by the limiter. The additional SOL region is homogeneous because all field lines end in both directions on the limiter. The total length of the field lines is about $4\,\text{m}$. The area with $R - R_0 > 13.5\,\text{cm}$, that means the former SOL, is named outer wall shadow (OWS). Here the length of the field lines is not homogeneous and defined by intersection with the vacuum vessel. Equilibrium profiles of the limited plasma were measured with the 1D and 2D manipulator from different outer ports. Significant differences between the profiles in the SOL region were revealed although the shape of the magnetic flux surfaces is supposed to be the same in both positions. These toroidal asymmetries are probably due to local plasma heating in the

Comparison of:		TJ-K	AUG
major plasma radius	R_0 (m)	0.6	1.65
minor plasma radius	a (cm)	5.5	50
tor. mag. field	B_t (T)	0.3	3.1
typical savety factor	q	3	3-5
plasma density	n ($10^{18}\ m^{-3}$)	0.5	100
electron temperature	T_e (eV)	10	20 k
ion temperature	T_i (eV)	<1	20 k

Table 3.1: Comparison of machine and plasma parameters in the limited TJ-K and ASDEX Upgrade

SOL. For this reason a second limiter plate was manufactured to separate plasma source and probe array toroidally by two plates. Thus in the future, the measurements can be repeated with two limiter plates and higher heating power (Chapter 8).

3.2 The tokamak ASDEX Upgrade

The tokamak ASDEX Upgrade (AUG) [21] is a fusion plasma device operated since 1990 at the Max-Planck-Institut für Plasmaphysik (IPP) in Garching near Munich. Its major and minor radius is 1.65 and 0.5 m, respectively. A detailed description of tokamaks can be found in Ref. [14]. Planar field coils generate the toroidal magnetic field of up to $B_t = 3.1$ T. Plasma currents of $0.4 - 1.4$ MA generate the poloidal field component. The plasma is usually kept in the lower single-null (LSN) magnetic configuration. This configuration with a single X-point at the bottom divertor is shown in Fig. 3.2. Beside Ohmic heating by the plasma current, additional systems of neutral beam injection (NBI), electron (ECRH) and ion-cyclotron-resonant heating (ICRH) are available. Working gases are hydrogen, deuterium and helium. Plasma densities of up to 10^{20} m^{-3} and temperatures of about 20 keV are achieved. This corresponds to temperatures of up to 250 million degree Kelvin. The pulse duration of the plasma discharges is up to 10 s. It is limited by the transformer inducing the plasma current. Machine and plasma parameters can be found in table 3.1. Unlike plasma devices with limiters defining the separatrix, the diverted AUG discharges easily transit from the low confinement mode (L-mode) into the high confinement mode (H-mode). This transition was observed first at IPP Garching in the 80s [22] and occurs usually in additional heated divertor experiments. High densities are achieved in the edge of H-mode plasmas because of a flow shear layer causing a transport barrier.

An extensive set of diagnostics is installed on AUG. Here, only those relevant for this work
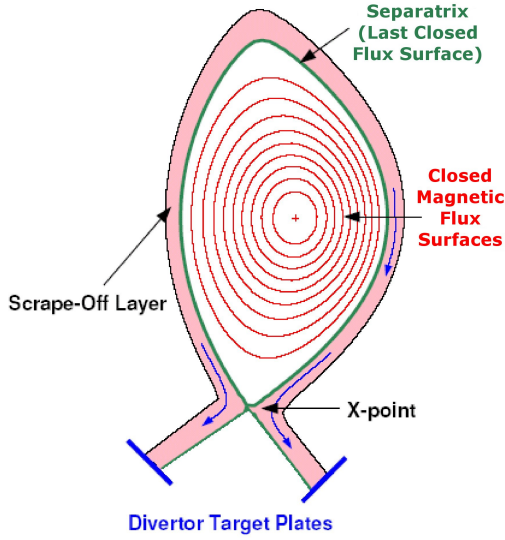
Figure 3.2: Magnetic flux surfaces in ASDEX Upgrade [23]. The last closed flux surface marks the transition from the confined plasma to the scrape-off layer.
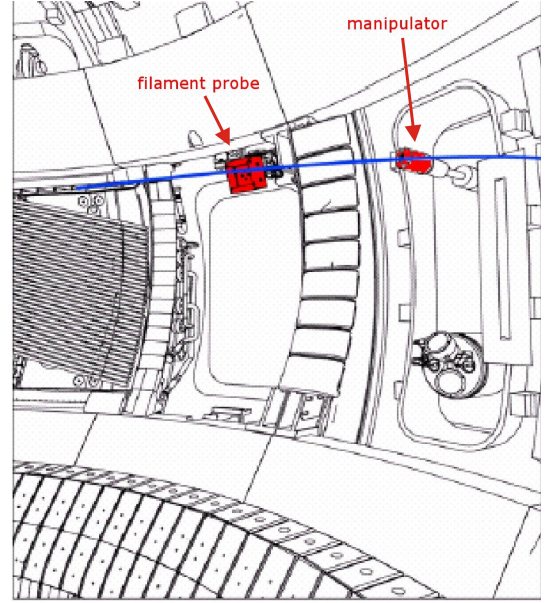
Figure 3.3: View into the vacuum vessel on mid-plane manipulator (MEM) and filament probe (F-Probe) [24]. Their magnetic connection is indicated by a fieldline.

are introduced. On the mid-plane manipulator (MEM) a reciprocating probe is installed, which moves the probe from outside the plasma into the SOL. During a discharge, typically two strokes of the probe are carried out, each of a duration of about 300 ms. Usually, it is not possible to move probes close to the separatrix, because the heat load would destroy the probe and pollute the plasma. A second probe system, the filament probe (F-probe) [25], is also a mobile device consisting of 9 Langmuir probes and a magnetic pic-up coil. For specific edge safety factors, the two probe systems are magnetically connected as shown in Fig. 3.3. The F-probe can therefore serve as a fixed reference with respect to the reciprocating probes on the MEM.

The lithium-beam diagnostic injects neutral lithium atoms with $15 - 100$ keV from the low field side into the plasma. The light emitted from this beam is captured with a radial resolution of about 5 mm. Based on these measurements the electron density profiles are calculated with a temporal resolution of several milliseconds [26]. The diagnostic is also used for charge exchange recombination spectroscopy (CXRS). This provides ion temperature profiles of the helium impurities in the plasma.

In this work, the SOL is divided into three different areas. Fig. 3.4 illustrates this division into divertor SOL (DSOL) ($R = 2.154 - 2.199$ m), limiter SOL (LSOL) ($R = 2.199 - 2.209$ m) and outer wall shadow (OWS) ($R > 2.209$ m). Magnetic field lines intersect in these areas with divertor plates, ICRH antennae limiters and vessel limiters, respectively. The total lengths of the field lines are given in the figure. The plasma density is extremely
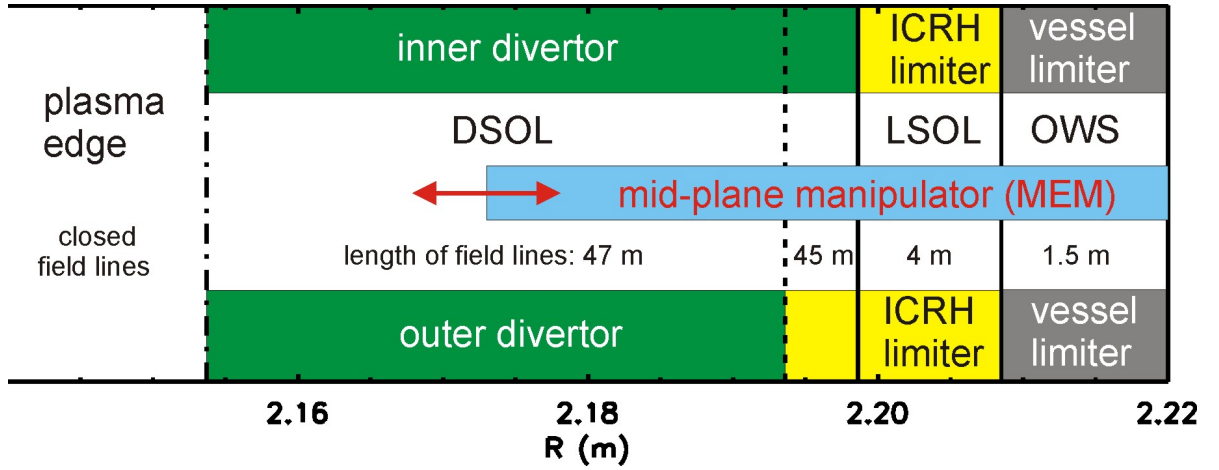
Figure 3.4: The SOL is divided into three parts: Divertor SOL (DSOL), limiter SOL (LSOL) and outer wall shadow (OWS). The radial position R corresponds to the mid-plane of the plasma. The field line limiting elements are indicated at top and bottom of the figure.

low in LSOL and OWS. The radial range of data represented in this work end at the beginning of the OWS, where the plasma is of no interest for the transport phenomena investigated here. Between DSOL and LSOL, there is a region of about 5 mm, where the field lines intersect the ICRH limiter in one and the inner divertor in the other direction.

3.3 Langmuir Probe Theory

For the investigation of the plasma parameters, mainly Langmuir probes were used. They provide access to plasma density, potential and electron temperature. In cylindrical geometry, a Langmuir probe consists of a wire isolated against the plasma except for a small tip, which provides good spatial resolution. Different bias voltages are applied to the pin and the current through the probe is measured. A typical probe circuit is shown on the left-hand side of Fig. 3.5. At bias voltages sufficiently negativ with respect to the pasma potential, the ion current saturates. Here the electrons are completely repelled. The ion-saturation current I_{sat} is proportional to the plasma density n and the square root of the electron temperature $\sqrt{T_e}$. With increasing bias voltage, more and more electrons can reach the probe. The electron current increases exponentially. At the so-called floating potential, the electron current cancels out the ion current and the net current to the probe is zero. The exponential increase of the electron current depends on the electron temperature T_e. T_e is obtained by fitting an exponential curve to the probe characteristics. The electron current increases further with the bias voltage until the plasma potential ϕ_p is reached and electrons of arbitrary energy can reach the probe. For a planar probe of infinite size, the electron current would saturate. In reality it keeps raising because the collection area increases with the sheath thickness. In magnetized
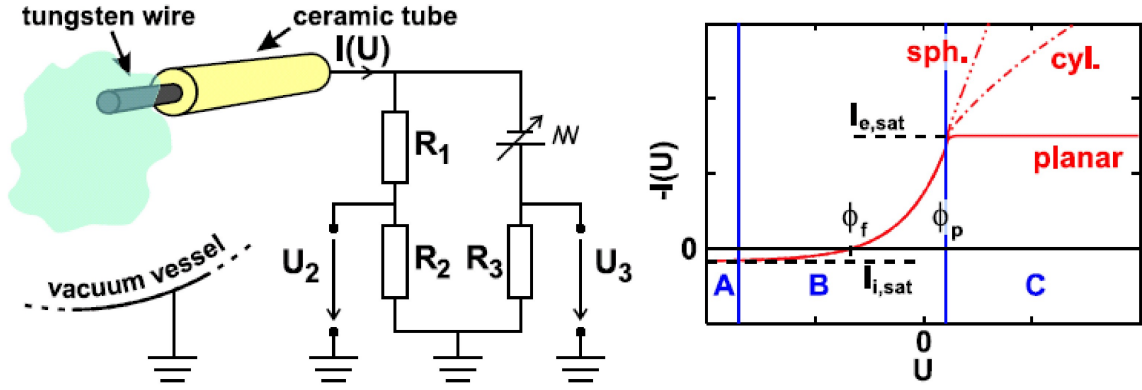
Figure 3.5: Principles of Langmuir probe measurements. Left: Probe circuit. U_2 measures the probe bias and U_3 the current response. Right: Characteristics of a Langmuir probe. Ion saturation current (A), transition region (B) and electron saturation range (C). Pictures are from [12].

plasma, probe theory becomes more complicated as the mobility of the particles is limited. For small probes as used in TJ-K, the effective probe surface S depends on the gyro radius. This affects essentially the calculation of abolut density values based on the characteristics. In this work, Langmuir probes are not used for absolute density measurements. Nevertheless, the probes are still applicable for fluctuation and qualitative profile measurements. The corrections of the simple probe theory for magnetized plasmas can be found in references [27, 28, 29].

For turbulence investigations, a high temporal resolution measurement of the fluctuating plasma parameters is necessary. For this reason probe pins are either used for I_{sat} or ϕ_{float} measurements. These parameters are accessible without knowledge of the entire probe characteristic. The floating potential is measured over a high resistance to the vacuum vessel without applying any bias voltage to the probe. Floating potential fluctuations are proportional to plasma potential fluctuations $\widetilde{\phi}_{float} \sim \widetilde{\phi}_p$ if the temperature fluctuations can be neglected. The validity of this assumption for TJ-K plasmas can be found profen in Ref. [30]. The relation of ϕ_{float} and ϕ_p is given by [1]

$$\phi_{float}^* = \phi_p - \frac{T_e}{2e} \ln \left(\frac{m_i T_e}{m_e T_i} \right) \tag{3.1}$$

for $T_i \approx T_e$ and

$$\phi_{float} = \phi_p + \frac{T_e}{e} \ln \left(0.61 \sqrt{2\pi \frac{m_e}{m_i}} \right) \tag{3.2}$$

for $T_i \ll T_e$. Here e is the elementary charge, m_i the ion and m_e the electron mass, T_i the ion and T_e the electron temperature. For high frequency fluctuation measurements of ϕ_{float}, it can be important to minimize cable capacity between probe and resistance [31], to avoid low pass filtering. In AUG this is not the case and in TJ-K the capacities are

small enough. Ion-saturation current fluctuations are proportional to density fluctuations $\widetilde{I}_{sat} \sim \widetilde{n}$ if the temperature fluctuations can be neglected. The ion current is given by [1]:

$$I_{sat}^* = enS\sqrt{\frac{T_i}{2\pi m_i}} \tag{3.3}$$

for $T_i \approx T_e$ and

$$I_{sat} = 0.61enS\sqrt{\frac{T_e}{m_i}} \tag{3.4}$$

for $T_i \ll T_e$. The bias voltage V_{probe} used for I_{sat} measurements was usually about $-100\,\text{V}$ with respect to the vacuum vessel. It has to satisfy the relation $V_{probe} \leq \phi_{float} - 2.3T_e/e$, to be sure that the ion current is sufficiently saturated. This may cause problems close to the separatrix of a fusion plasma where ϕ_{float} becomes strongly negative. Another limit to Langmuir probe measurements in hot plasmas is imposed by thermal load. Hot Langmuir pins start electron emission before they are distroyed. Such a negative electron current leads to an overestimation of I_{sat}. Emitting probes can be used to measure the plasma potential directly ($\phi_{float} \approx \phi_p$).

3.4 8-Pin Probe at TJ-K

A poloidal probe array has been constructed for turbulence studies at TJ-K. It consists of 8 Langmuir probes, which can be seen in Fig. 3.6. Each probe pin consists of a tungsten wire of 2 mm length and 200 μm diameter. The insulating ceramics tube has a diameter of 1 mm. The probes are mounted at a poloidal distance of 5 mm in an aluminum support. The 8-pin probe is mounted on the 2D manipulator. The total length of the probe array is 477 mm and enables investigation in a wide range of the poloidal cross section. Small pieces of copper wire have been welded at the ends of the tungsten wires to enable soldering them into the plugs. A fixed single reference probe of the same type is installed at $r = R - R_0 = 10,5\,\text{cm}$ in a toroidal distance of 1 cm to the 8-pin probe (Fig. 3.6). A band-pass filter of $1 - 300\,\text{kHz}$ is a applied to the signals before they are amplified by a Textronix AM502 amplifier and transmitted to the Nicolet multichannel recording system. The fluctuation signals are acquired with 16 bit depth and 1 MHz sampling rate per channel. For ion-saturation current (I_{sat}) measurements, a bias voltage of $-90\,\text{V}$ is applied to the probes. I_{sat} is measured with pins 1, 2, 4, 6, 7 in top to bottom order and the reference probe. The floating potential is measured with pins 3 and 5. AC and DC measurements are carried out in separate discharges at the same discharge parameters.

3.5 14-Pin Probe at AUG

A Langmuir probe array for turbulence investigations in ASDEX Upgrade (AUG) was designed and constructed in cooperation. The result is shown as a schematic view in Fig. 3.7 and as a picture on the left-hand side of Fig. 3.8. It is suitable for the mid-plane manipulator (MEM) in AUG. Each pin consists of a graphite tip hard soldered to the connecting wire inside an insulating ceramics tube and shielded against electromagnetic waves. In fusion plasmas usually carbon probes are used. In presence of high particle and heat flows, a carbon pin sublimates and the arising carbon cloud cools the plasma around the pin. Metal pins pollute the plasma much more by sputtering and melting pins can not protect themselves. A metal pin is lost, if it melt once, because arising sharp edges will cause arcing in following discharges. The pins of the 14-pin probe were manufactured at IPF Stuttgart and some of them can be seen on the right-hand of Fig. 3.8. The pins are mounted on three different levels in the graphite probe head. The collecting part of the probe is a cylinder with diameter $0.9\,mm$ standing $2\,mm$ over the probe body. The top level of the probe head has two parallel rows with 5 and 4 pins. The distance between two pins perpendicular to the magnetic field is $2.75\,mm$, if the main level of the probe is mounted perpendicular to the field lines in the torus. The 5 low level pins permit the investigation of radial correlations and the use as a Mach probe. The massive graphite probe head sustains high heat and particle load and offers a low level of plasma contamination. During the measurements in October 2007, the angle between field lines and probe array was about $80°$ due to mechanical difficulties. This led to a non equidistant pin distribution perpendicular to the magnetic field that had to be considered in the data analyses.

The signals measured by the different probe pins during discharges #22504 and #22505 are indicated in Fig. 3.7. The high poloidal resolution of $2.75\,mm$ is dedicated to small scale turbulence investigation. The large poloidal extension of $22\,mm$ is necessary for parallel correlation measurements with the fixed filament probe as reference (see Fig. 3.3).

Four probes were biased to $-80\,V$ by Kepco power supplies and two probes were biased to $-160\,V$ by accumulator blocks. Measurements were carried out with the so-called Hotlink system at AUG and acquired with $16\,bit$ at $2\,MHz$. A fourth order low-pass filter with a cut-off frequency of $700\,kHz$ was applied prior to acquisition. The probe can stroke several times per discharge into the plasma. During one discharge, all strokes have the same maximum stroke position. The time, during which the probe stands fixed at the maximum stroke position, is called ramp. The ramp is fixed to one value for all strokes during a discharge. It is usually chosen between 1 and $200\,ms$. The reciprocation speed is fixed. The inward and outward motion take about 40 and $90\,ms$, respectively.
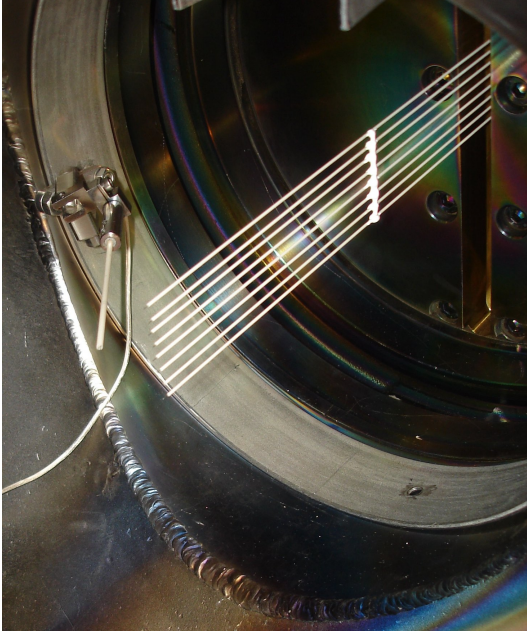
Figure 3.6: View on the mobile 8 pin probe and fixed reference probe inside the TJ-K vessel.
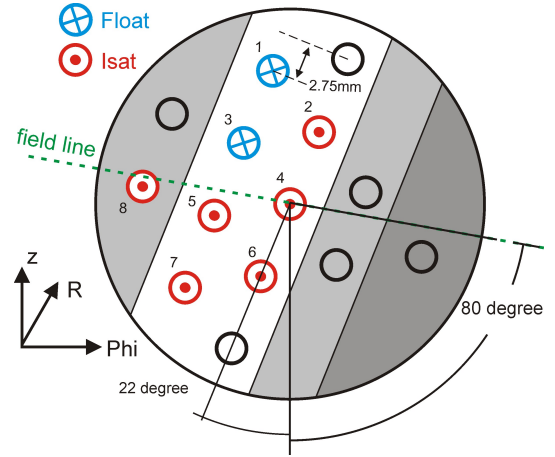

Figure 3.7: View from the plasma on the 14-pin probe. Probes 1 and 3 measure the floating potential, probes 2 and 4 to 8 measure the ion-saturation current. The dashed line indicates the direction of the magnetic field lines.

Figure 3.8: Left: Head of the 14 pin Langmuir probe array built for the mid–plane manipulator in AUG. Right: Carbon pins hard soldered inside the insulating ceramics tube to resist high heat fluxes from the plasma.

Chapter 4

Dimensional Similarity

Plasma turbulence simulation codes gain in importance to predict plasma scenarios in future fusion devices. Numerical simulations have to be cross-checked with experimental results to assure that the model is valid. For parameters typical for the edge of fusion plasmas, the most detailed comparative studies on a microscopic level have been carried out on TJ-K. For comparison with turbulence measurements, the DALF3 code [32] has been used. The simulation results, predicting drift-wave turbulence, were found to be in good agreement with experimental findings in TJ-K [9, 10, 33]. The dynamics in the model is controlled by non-dimensionally parameters. Plasma discharges with the same non-dimensional parameters are called dimensional similar. The low-temperature plasma in TJ-K is dimensionally similar to the SOL of hot fusion plasmas [11]. The relevant non-dimensional parameters are introduced in section 4.1. Section 4.2 compares non-dimensional and general plasma parameters of limited TJ-K plasmas with the SOL of ASDEX Upgrade.

4.1 Non-Dimensional Plasma Parameters

The relevant non-dimensional parameters are the normalized ratio of thermal and magnetic energy β^*, the normalized collisionality ν^* and the normalized electron-ion mass ratio μ^*. The normalized ratio of thermal and magnetic energy is given by

$$\beta^* = \mu_0 \frac{n_e T_e}{B^2} \left(\frac{q_s R_0}{L_\perp} \right)^2 . \tag{4.1}$$

The collisionality is normalized by

$$\nu^* = 0.51 \nu_e \frac{L_\perp}{c_s} \tag{4.2}$$

with the electron collision rate

$$\nu_e = \left(\frac{e^2}{4\pi\epsilon_0} \right)^2 \times \frac{8\pi \ln \Lambda(n_e, T_e)}{3\sqrt{3 m_e}} \times \frac{n_e}{T_e^{3/2}} \tag{4.3}$$

The normalized mass ratio is

$$\mu^* = \frac{m_e}{M_i} \left(\frac{q_s R_0}{L_\perp} \right)^2 . \tag{4.4}$$

The parameters necessary for these calculations are electron density n_e [m^{-3}] and temperature T_e [eV], magnetic field B [T], safety factor q_s, major radius R_0 [m], elementary charge e [C], permeability μ_0 [H/m] and permittivity ϵ_0 [F/m] of free space, electron and ion mass, m_e and M_i [kg]. $L_\perp$ [m] is the perpendicular density gradient scale length:

$$L_\perp = \left| \frac{n_e}{\nabla n_e} \right| = |\nabla \ln(n_e)|^{-1} . \tag{4.5}$$

c_s [m/s] is the ion sound speed defined as $c_s = \sqrt{T_e/M_i}$ and $\ln \Lambda$ is the Coulomb logarithm, which can be approximated by [34]

$$\ln \Lambda = 30.3 - 1.15 \log_{10}(n_e) + 3.45 log_{10}(T_e) \text{ for } T_e < 50\,\text{eV}, \tag{4.6}$$

$$\ln \Lambda = 32.2 - 1.15 \log_{10}(n_e) + 2.30 log_{10}(T_e) \text{ for } T_e > 50\,\text{eV}. \tag{4.7}$$

4.2 Comparison of TJ-K and AUG Parameters

The plasma parameters have been calculated at specific radial positions in TJ-K and ASDEX Upgrade. The results are compared in table 4.1.

In TJ-K, the parameters were determined for hydrogen and helium discharges with high and low magnetic field, for the configuration with the limiter inserted. At low magnetic field, two radial positions were examined. In both gases, one position was chosen close to the last closed flux surface (LCFS) and the other in the scrape-off-layer (SOL). At high magnetic field only one position was examined per discharge. This position was chosen in the steepest density gradient. The input parameters were taken from the limited hydrogen discharges #4636 and #4638 and the limited helium discharges #4639 and #4641. More details of these discharges are presented in chapter 6.

It must be stressed, that the dimensionless parameters in TJ-K are different for the case with and without limiter. However, it has been shown that the fluctuations inside the separatrix show in the limited case still drift-wave characteristics [16]. The dynamics changed across the separatrix from drift-wave to interchange like turbulence. Only limited TJ-K discharges are compared with AUG discharges in this work.

In ASDEX Upgrade, the parameters were determined at three different radial positions. One position was chosen in the strong density gradient of the inner DSOL and the other two in central and outer DSOL. The investigation is based on the Ohmic L-mode discharges #22504 and #22505, that are presented in chapter 7.

experiment	AUG	AUG	AUG	TJK	TJK	TJK	TJK	TJK	TJK
mag. field lines	inner DSOL	central DSOL	outer DSOL	LCFS	SOL	LCFS	SOL	SOL	SOL
gas	D	D	D	H	H	He	He	H	He
safety factor q_s	3.9	3.9	3.9	3.	3.	3.	3.	3.	3.
major radius R_0 (m)	1.65	1.65	1.65	0.6	0.6	0.6	0.6	0.6	0.6
radius R (cm)	217.0	217.6	218.3	69.0	73.0	69.0	73.0	71.0	68.0
tor. mag. field B_t (mT)	1521.	1517.	1512.	63.	59.	63.	59.	233.	244.
density n(10^{17} m^{-3})	13.0	10.0	7.2	0.5	0.1	0.6	0.2	0.6	0.9
scale length $L_\perp$ (cm)	1.0	2.8	2.8	2.4	4.1	2.1	3.7	2.0	2.5
el. temp. T_e (eV)	12.	10.	10.	7.	10.	11.	13.	7.	10.
el. gyro rad. r_e (mm)	0.005	0.005	0.005	0.101	0.127	0.126	0.145	0.027	0.031
ion temp. T_i (eV)	60.	50.	10.	1.	1.	1.	1.	1.	1.
ion gyro rad. r_i (mm)	0.73	0.67	0.30	1.63	1.72	1.63	1.72	0.44	0.42
sound speed C_s (km/s)	59.	54.	31.	28.	32.	17.	18.	28.	16.
drift scale ρ_s (mm)	0.3	0.3	0.3	4.3	5.5	10.8	12.4	1.2	2.7
norm. plasma beta β^*	**0.562**	0.046	0.033	**0.101**	0.011	**0.249**	0.026	0.013	0.016
norm. mass ratio μ^*	112.95	14.41	14.41	3.07	1.05	1.00	0.32	4.42	0.71
norm. collison rate ν^*	**0.28**	0.86	1.07	**0.12**	0.02	**0.11**	0.04	0.12	0.23

Table 4.1: Comparison of plasma parameters in ASDEX Upgrade and TJ-K.

Most absolute parameters are quite different between TJ-K and ASDEX Upgrade. Magnetic field strength, plasma density and ion temperature in AUG are over 25 times larger than in TJ-K. Large differences of the normalized mass ratios are due to the different major radii. The normalized parameters β^* and ν^* differ only by a factor of $2-6$ between the inner-DSOL of AUG and the LCFS in TJ-K. In table 4.1, the corresponding values are printed in bold. Similar factors are found for β^* in central-DSOL and the SOL of TJ-K low-magnetic field discharges. Regarding the large scatter of the non-dimensional parameters between different plasma discharges, the dynamics of limited TJ-K discharges are expected to be comparable to the SOL of AUG. The investigation of plasma dynamics in the two devices is presented in the following two chapters. Similarities and differences of both experiments are discussed in chapter 8.

Chapter 5

Data Analyses

This chapter presents the methods, which are applied to data from TJ-K and AUG in chapters 6 and 7. Section 5.1 describes the data acquisition and pre-treatment in both devices. The investigation of the statistical properties is introduced in section 5.2. Correlation analyses and the determination of radial transport are shown in sections 5.3 and 5.4, respectively.

5.1 Raw data

In TJ-K, fluctuations were measured spatially point by point. Up to 10^6 data points were acquired per position with a sampling rate of 1 MHz. Data analyses were performed with the entire time traces in order to guarantee good statistics. The radial extent of the pobe pins is 2 mm and the ion-gyro radius about 2 mm. Therefore, the uncertainty in the radial position of the measurements is estimated to ± 3 mm, with respect to the pin centre.

In ASDEX Upgrade, the probes move continuously during the probe strokes into the plasma, while the signals are acquired. In this work, only data from the inward motion are used, since they are supposed to be least perturbed by interaction of the probe head with the plasma. Moreover, these signals showed an excellent reproducibility. Fig. 5.1 exemplarily shows the raw signals of I_{sat} and ϕ_{float} during an inward motion of the probe. Starting at $t = 1.6$ s, the probe moves in the first 20 ms about 55 mm towards the separatrix until it reaches its final position at $R = 2.16$ m. The results represented in chapter 7 are based on time traces of about 18 ms duration. With the aquisition rate of 2 MHz, this corresponds to 3.6×10^4 data points per stroke and channel. With a pin length of 2 mm and ion-gyro radii $r_i < 1$ mm, the radial uncertainty is about ± 2 mm.

For the statistical analyses, the AUG time traces are subdivided into series of 4096 data points with an overlap of 2048 points. Each series corresponds to about 2 ms and a radial range of 5.5 mm. The mean signal and the mean radial position of each series
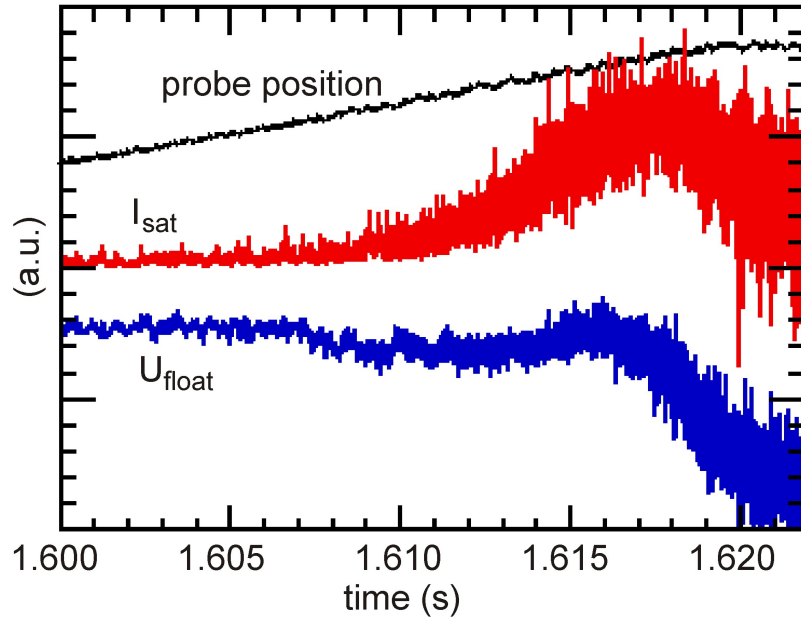
Figure 5.1: Raw data from the first probe stroke in discharge #22505 at AUG. Top: Probe position during inward motion $R = 2.21 - 2.16$ m; Middle: I_{sat} signal; Bottom: ϕ_{float} signal;

are calculated. All mean signals of different pins, which are assigned to the same radial interval within a 3 mm grid, are averaged for the equilibrium profiles of I_{sat} and ϕ_{float}. The relative fluctuations ($\tilde{x}/ <x>$) of all series, which are assigned to the same radial interval within the 3 mm grid, are joined to long time traces. Based on these relative fluctuation time traces, the radial profiles of the PDF and its moments are determined.

For correlation analyses, the initial AUG signals are subdivided into series of 2048 data points, with an overlap of 512 points. This corresponds to about 1 ms. In this time, the probe moves almost 3 mm. In the figures based on correlation analyses, the result of each series is plotted. This leads to much more plotted points per discharge because no series were merged in this case.

Fig. 5.2 shows 60 μs of fluctuating signals measured in ASDEX Upgrade. The exact position of each probe pin is indicated in Fig. 3.7. Turbulent events are observed to move poloidally upward from high to low pin numbers. Some of these structures are marked by diagonal lines. The following sections describe the methods employed to characterize such fluctuating signals from TJ-K and ASDEX Upgrade.

5.2 Statistical Properties

The probability to find in a fluctuating signal a certain amplitude is given by the probability density function (PDF). It characterizes the fluctuation data measured for example with
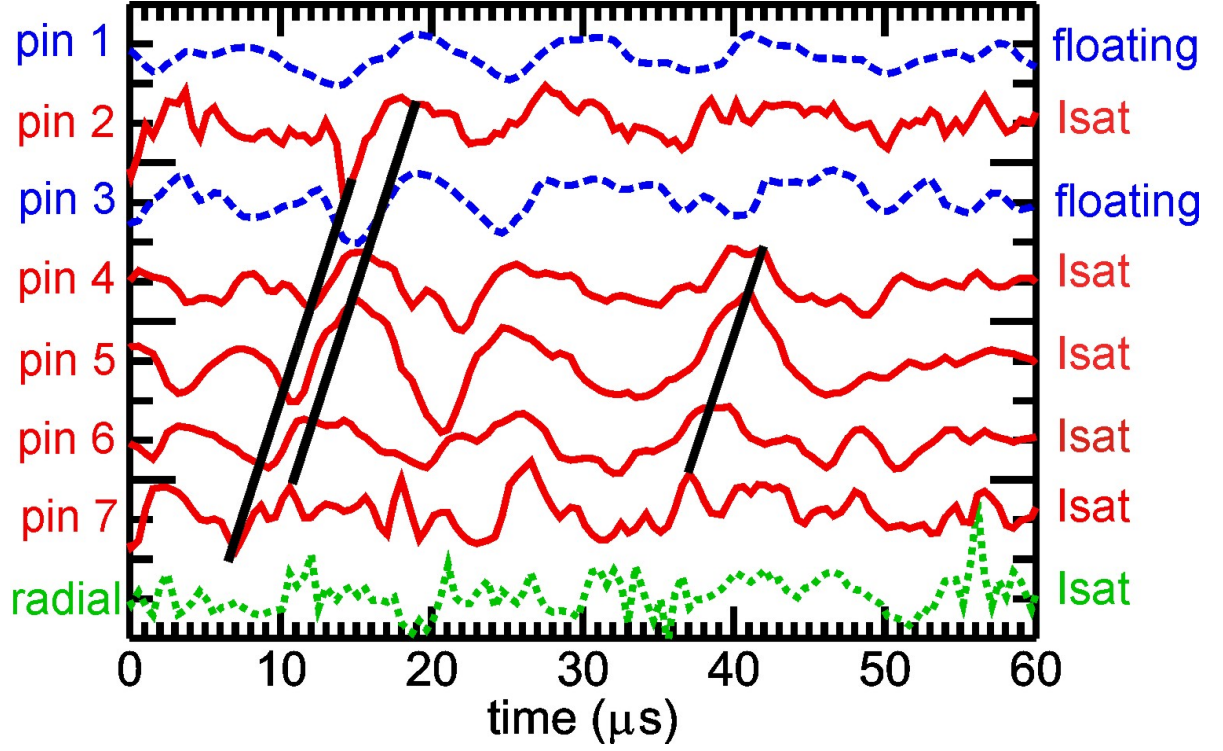
Figure 5.2: Comparison of 60 μs raw data measured with the 14-pin probe in AUG. Pin numbers are the same as in Fig. 3.7. The poloidal upward motion of quasi coherent structures is indicated with diagonal lines.

a probe. The PDF of a normally distributed, i.e. Gaussian signal is given by

$$P_N(x) = \frac{1}{\sigma_x\sqrt{2\pi}} \exp(-\frac{(x - \langle x \rangle)^2}{2\sigma_x^2}). \tag{5.1}$$

The statistical moments mean value, standard deviation, skewness and kurtosis characterize the PDF in general. In the present work, the statistical moments are analyzed to compare plasma fluctuations in TJ-K and the SOL of ASDEX Upgrade. Here the measured quantity, in the present case I_{sat}, is represented by the random variable x. It may be split up in into a constant DC and a fluctuating AC part $x = x_0 + \tilde{x}$. The mean value $\langle x \rangle = x_0$ defines the DC background level of the signal x. It is given by

$$\langle x \rangle = \int_{-\infty}^{+\infty} x\, P(x)\, \mathrm{d}x \approx \frac{1}{N} \sum_{i=0}^{N-1} x_i. \tag{5.2}$$

The variance σ_x^2 is given by

$$\sigma_x^2 = \langle (x - \langle x \rangle)^2 \rangle = \int_{-\infty}^{+\infty} (x - \langle x \rangle)^2 P(x)\mathrm{d}x \approx \frac{1}{N-1} \sum_{i=0}^{N-1} (x_i - \langle x \rangle)^2. \tag{5.3}$$

The relative fluctuation level expresses the importance of the fluctuation amplitude compared to the DC background level. It is given by the relative standard deviation $\sigma_x/\langle x \rangle$.

The shape of a PDF is characterized by normalized versions of the third and fourth moments $m_k \equiv \langle (x - \langle x \rangle)^k \rangle$, $k = 3, 4$. The skewness S is a measure for the asymmetry of the PDF and is given by

$$S \equiv \frac{m_3}{m_2^{3/2}} \approx \frac{1}{N} \sum_{i=0}^{N-1} \left(\frac{x_i - \langle x \rangle}{\sigma_x} \right)^3. \tag{5.4}$$

Compared to a Gaussian PDF ($S = 0$), a positive or negative skewness indicates an asymmetry in the direction of positive or negative x values, respectively. The peakedness of a probability distribution is given by the kurtosis

$$K \equiv \frac{m_4}{m_2^2} - 3 \approx \left\{ \frac{1}{N} \sum_{i=0}^{N-1} \left(\frac{x_i - \langle x \rangle}{\sigma_x} \right)^4 \right\} - 3. \tag{5.5}$$

With respect to a Gaussian PDF ($K = 0$), a positive kurtosis indicates a more peaked maximum with the tails having a weaker slope. Negative values indicate a comparatively flat maximum and a stronger slope of the tails.

5.3 Correlation Analyses

Correlation analyses are used to investigate the correlation, i.e. the similarity between fluctuating signals. In turbulence investigations, they are used to detect and characterize coherent structures. Characteristic time and length scales of the turbulence are identified. The propagation of such structures is indicated in Fig. 5.2. Cross-correlation analyses supply an effective tool, to determine the mean phase velocity of a structure from a whole time trace.

The cross-correlation function of two signals $\tilde{x}$ and $\tilde{y}$ is defined by

$$C'_{x,y}(\tau) = \int \tilde{x}(t) \tilde{y}(t + \tau) dt = \int \tilde{x}_\omega \tilde{y}_\omega^* \exp(i\omega\tau) d\omega. \tag{5.6}$$

The normalized cross-correlation function

$$C_{x,y}(\tau) = \frac{C'_{x,y}(\tau)}{\sqrt{C'_{x,x}(0) C'_{y,y}(0)}} \tag{5.7}$$

is limited to the range $[-1, +1]$. A correlation level of $C_{x,y}(\tau) = +1$ is obtained from identical signals. The cross-correlation of two different white noise signals is $C_{x,y}(\tau) = 0$, i.e. they are not correlated at all. $C_{x,y}(\tau) = -1$ indicates anti-correlated signals.

$C_{x,x}(\tau)$ is the auto-correlation function. It is always $C_{x,x}(0) = +1$, even if the signal is white noise. Fig. 5.3 shows a typical auto-correlation function $C_{x,x}(\tau)$ based on an I_{sat}
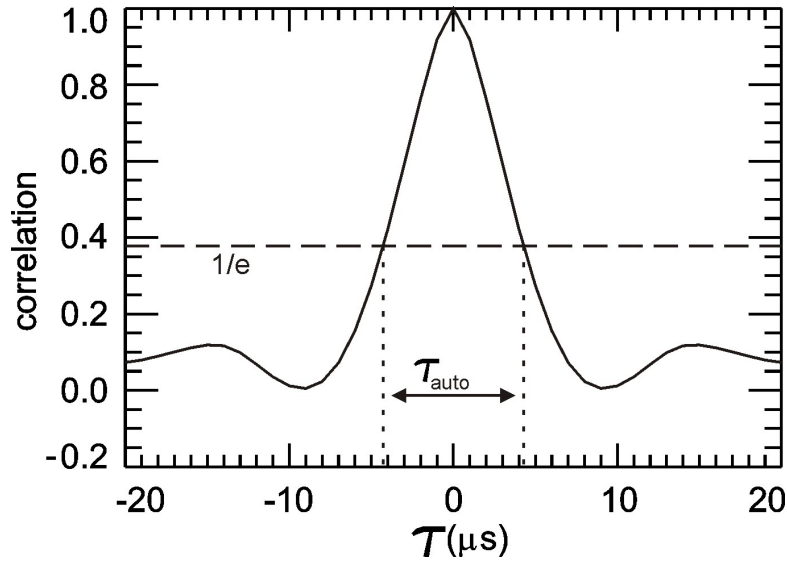
Figure 5.3: Auto-correlation function of an I_{sat} signal from AUG. The width of the function at the correlation level $1/e$ gives the auto-correlation time τ_{auto}.

signal from AUG. The auto-correlation time τ_{auto} is defined as the $1/e$-folding time of the auto-correlation function. τ_{auto} is the duration, in which the signal stays considerably large.

From poloidally separated probes one can determine the poloidal propagation speed of structures based on cross-correlation analyses. The left side of Fig. 5.4 shows the cross-correlation functions of four poloidally separated probes in AUG. Probe number five is the reference. Here the auto-correlation function at $\tau = 0$ is 1. A temporal shift $\Delta\tau$ is observed between the other correlation maxima. Coherent structures propagate poloidally from probe number six to probe number two. The structure is first measured at probe number six ($\Delta\tau < 0$), arrives at the reference probe number five ($\Delta\tau = 0$) and moves further to lower probe numbers ($\Delta\tau > 0$). According to the sampling rage of 2 MHz, the resolution of τ is 0.5 µs. This time resolution leads to discrete poloidal velocities. A parabola is fitted to the peak of each correlation function to avoid discrete values by interpolation of the maximum. The poloidal propagation velocity v_θ of the coherent structures is then given by

$$v_\theta = \frac{d_\theta}{\Delta\tau}, \tag{5.8}$$

where d_θ is the poloidal distance of the probes. This relation is a good estimate as long as the poloidal phase velocity is much bigger than the radial one $v_\theta \gg v_r$. Geometrical considerations show that the ratio between measured ($\Delta\tau_{mes}$) and real poloidal propagation time between two pins ($\Delta\tau_{real}$) is given by

$$\frac{\Delta\tau_{mes}}{\Delta\tau_{real}} = \cos\alpha, \tag{5.9}$$

if the structure is circular and α is the deviation from a pure poloidal propagation. For a pure poloidal motion $\alpha = 0$ and $\Delta\tau_{mes} = \Delta\tau_{real}$. In this case, the measured velocity is correct and independent of the structure shape. For a pure radial motion $\alpha = \pi/2$ and $\Delta\tau_{mes} \approx 0$. In this case, the poloidal velocity is overestimated and its sign is influenced by the shape of the structure. The error in $\Delta\tau_{mes}$ depends on the ratio between v_θ and v_r. It has been found, that the relative error of v_θ remains below 10% as long as $v_\theta \geq 2 \times v_r$. This relation is supposed to be fulfilled in the present measurements, except for the separatrix position. The v_θ values shown in section 7.3 are taken from cross-correlations between probe pins 6 and 7. These probes are radially the closest to the plasma core.

The cross-correlation of different probes at $\tau = 0$ are used to examine the poloidal extent of the coherent structures (Fig. 5.4, left). The level of correlation decreases with increasing distance to the reference probe. The distance l, at which the correlation is $1/e \approx 0.37$ is taken as half of the poloidal correlation length of the structure, i.e. $L_\theta = 2 \cdot l$. Therefore, the correlation levels are linearly interpolated. Examples are shown on the right side of Fig. 5.4. The half correlation length is found in the range $l = 5 - 6\,\text{mm}$ for all three pins. This simple evaluation is not sensitive to the structures shape and errors occure for structures with a broad kernel and steep flanks or when the cross-correlation level is far from $1/e$. In the example shown on the right-hand side of Fig. 5.4, L_θ varies only slightly when different pins are considered for interpolation. The L_θ values presented in section 7.3 are based on cross-correlation analyses of probe pins number 6 and 7, only.
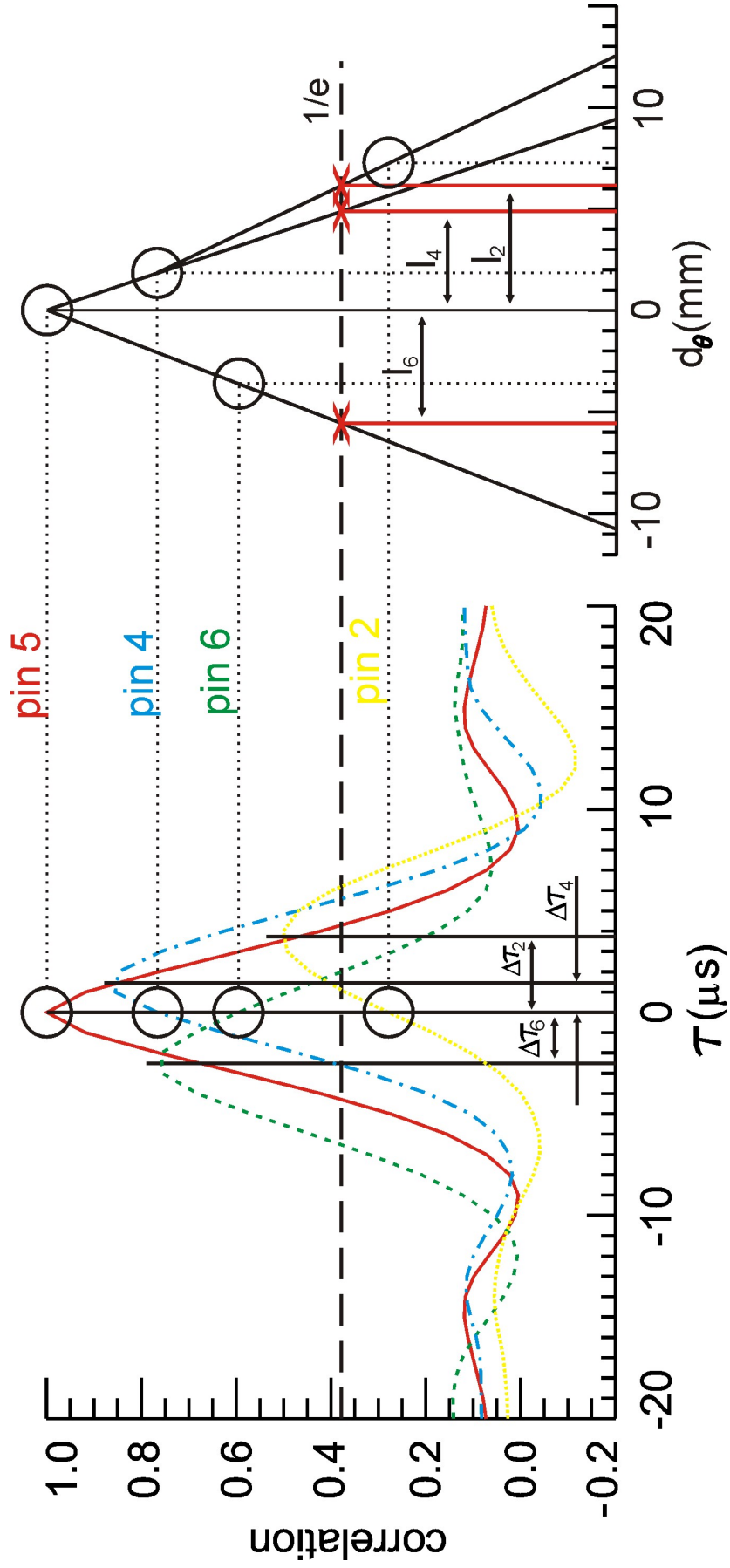
Figure 5.4: Left: I_{sat} cross correlation functions of probe numbers 2, 4 and 6 with the reference probe number 5. The position of the maximum defines $\Delta\tau$ to calculate the propagation velocity. Right: The cross correlation level at $\tau = 0$ plotted over the distance to the reference probe (pin 5). Linear interpolation gives the structure size $L_\theta = 2 \cdot l$ at the correlation level $1/e$.

5.4 Radial Transport

The local mean radial transport is investigated using poloidally slightly separated Langmuir probes. The floating potential is measured at the top (ϕ_1) and bottom (ϕ_2) probe. The central probe measures $\tilde{n} \sim \tilde{I}_{sat}$. From these measurements, the local mean transport Γ is estimated. The poloidal electric field fluctuations are given by $\tilde{E}_\theta \sim \tilde{\phi}_2 - \tilde{\phi}_1$. The underlying model was introduced in section 2.3. The cross phase determining the direction of transport is calculated according to [35]

$$\cos(\varphi) = \frac{\Gamma}{\sigma_{E_\theta}\sigma_n} = \frac{\left\langle \tilde{E}_\theta(t)\tilde{n}(t) \right\rangle_t}{\sigma_{E_\theta}\sigma_n}. \tag{5.10}$$

The sign of the transport is already included in the expression for the net radial transport

$$\Gamma = \frac{\left\langle \tilde{E}_\theta(t)\tilde{n}(t) \right\rangle_t}{B}. \tag{5.11}$$

Chapter 6

Experimental Results of TJ-K

Results on extensive turbulence studies carried out previously on plasmas in TJ-K can be found in Refs. [12, 13, 16, 17, 18, 36, 37]. The present investigation aims at the detailed comparison of electrostatic fluctuation properties in TJ-K and the edge of a fusion plasma. Due to the dimensional similarity of both plasmas, the properties are expected to be similar [10, 11]. In TJ-K, a poloidal limiter is applied to focus on the transition in the dynamics from the confined region to the SOL. Previous investigations [16] are extended to plasmas with 8.25 GHz ECRH. Discharges at low ($B = 70$ mT, 2.45 GHz) and high magnetic field ($B = 0.3$ T, 8.25 GHz) have been analyzed. The results are presented under the aspects of dimensional similarity in order to compare them directly with those obtained from the fusion device ASDEX Upgrade in chapter 7. The first section in this chapter shows equilibrium profiles of hydrogen and helium discharges for both magnetic fields. In section 6.2 the radial dependence of the PDF, and in section 6.3 the correlation analyses are presented. Section 6.4 summarizes and discusses the results from this chapter.

6.1 Equilibrium Profiles

Equilibrium profiles are used to determine radial gradients of potential, density and temperature. These gradients are necessary to estimate the background plasma drifts. This section presents radial profiles measured in limited TJ-K discharges with different gases and magnetic fields.

For hydrogen (#4636) and helium (#4639) plasmas at low magnetic field, the profiles are shown in Fig. 6.1. The floating potential profiles shown on the top indicate values of about $+1$ V in both cases at the end of the outer wall shadow (OWS) far from the plasma. Still in the OWS but closer to the scrape-off layer (SOL), they reach negative values of more than -2 V. These minima are followed by continuous potential increases throughout the SOL reaching their maxima of about $+4$ V one to two centimeters into

the confined plasma core. For both gases, the radial electric field at the separatrix is about 1.3 V/cm, hence they are rather weak in TJ-K plasmas. In the first centimeter of the SOL a stronger field of 2.9 V/cm is observed in the helium discharge, while the field in hydrogen remains constant. For $10\,\text{cm} \leq R - R_o \leq 13.5\,\text{cm}$ a value 0.6 V/cm is measured for both gases. For $r \geq 16\,\text{cm}$, ϕ_{float} has the same level. Neither the separatrix position nor the beginning of the outer wall shadow are clearly pronounced in the floating-potential profile. However, the positions might be indicated by smooth transitions in their vicinity within 2 cm.

The density profiles of hydrogen and helium 2.45 GHz discharges are shown in the middle of Fig. 6.1. Note the logarithmic density axis which has been chosen for a better visibility of the profiles in the SOL. The density decay length is about 2 cm close to the separatrix and 4 cm at the transition from the SOL to the OWS (see Tab. 4.1 for details). The electron temperature profiles are shown at the bottom of the same figure. T_e is found to be almost constant in plasma core and SOL with values around 8 and 11 eV for hydrogen and helium, respectively.

Fig. 6.2 shows the equilibrium profiles at the high magnetic field. They were measured in the limited discharges #4638 (H) and #4641 (He). The floating potential is shown at the top. In the plasma core it was found around +5 V for hydrogen and helium. Close to the separatrix position, maxima occur followed by a potential decrease throughout the SOL. Minima of −0.7 and −2.7 V for hydrogen and helium, respectively, are observed at the transition from the SOL to the OWS. The potentials increase again in the OWS with local maxima in this region. These potential differences cause radial electric fields in the SOL of about 1.6 V/cm for hydrogen and up to 3.5 V/cm for helium discharges. In the OWS, negative electric fields of −0.45 V/cm (H) and −2.3 V/cm (He) are observed. The maximum ion-saturation current at high magnetic field, middle) is less than half of I_{sat} at low magnetic field, but normalization to the interferometer density yields similar values for the core density (Fig. 6.2. For both gases a pedestal is found, but their positions differ from 2 cm inside the plasma core (He) to 1 cm outside the nominal separatrix (H) position. The density decay length next to the pedestal is 4.4 cm in the hydrogen and 6.1 cm in the helium discharge. The electron temperature at the bottom of Fig. 6.2 is constant around 8 eV for hydrogen. In helium discharges, T_e is found close to 10 eV in the confined plasma and reaches over 15 eV in the SOL. This maximum is possibly due to a localized energy deposition of the ECRH power in the SOL. Since the field lines are not closed, the thermal energy cannot equilibrate on a flux surface. Such direct influences will be avoided in future measurements using a second limiter to separate probe and heating system.
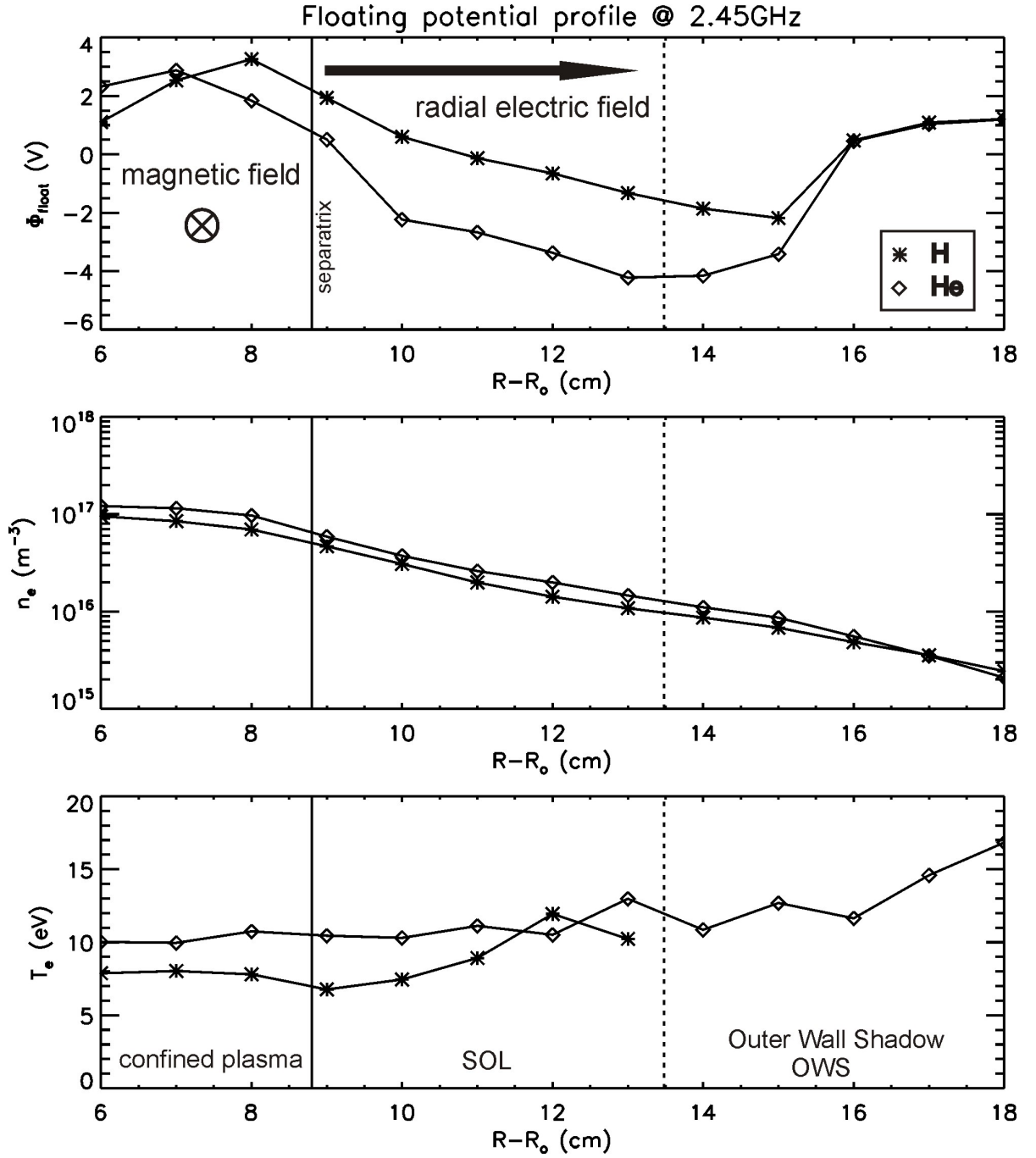
Figure 6.1: Floating potential (top), density in log scale (middle) and electron temperature profiles (bottom) of TJ-K hydrogen (stars) and helium discharges (diamonds) at low magnetic field. The radial range is divided into three parts: plasma core with closed field lines, SOL with homogeneous field lines leading to the limiter plate and the outer wall shadow (OWS) with inhomogeneous field lines leading to the vacuum vessel. The separatrix is indicated by a solid line and the boundary between SOL and OWS by a dashed one.
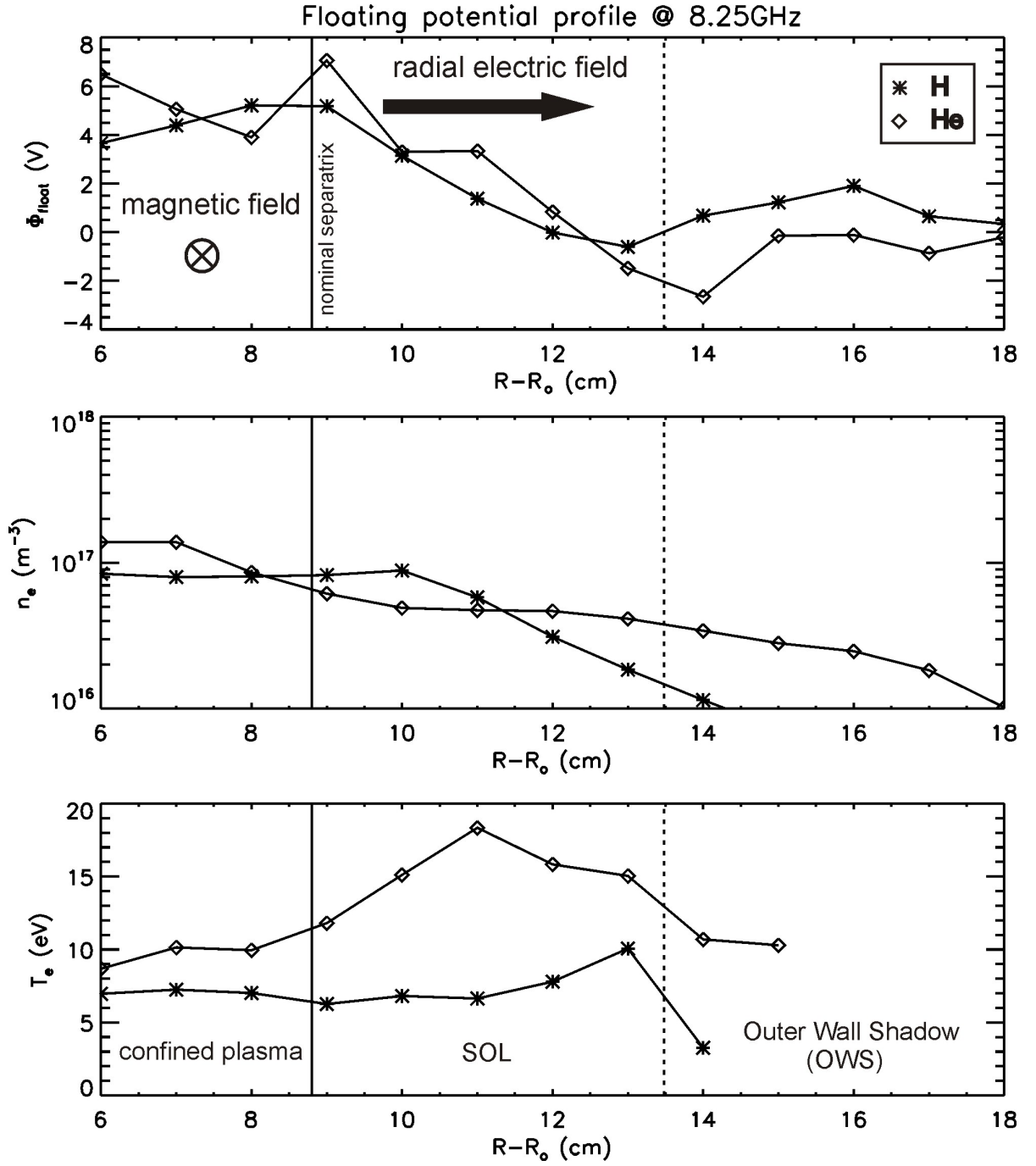
Figure 6.2: Profiles of TJ-K hydrogen and helium discharges at high magnetic field. The representation is the same as in Fig. 6.1.
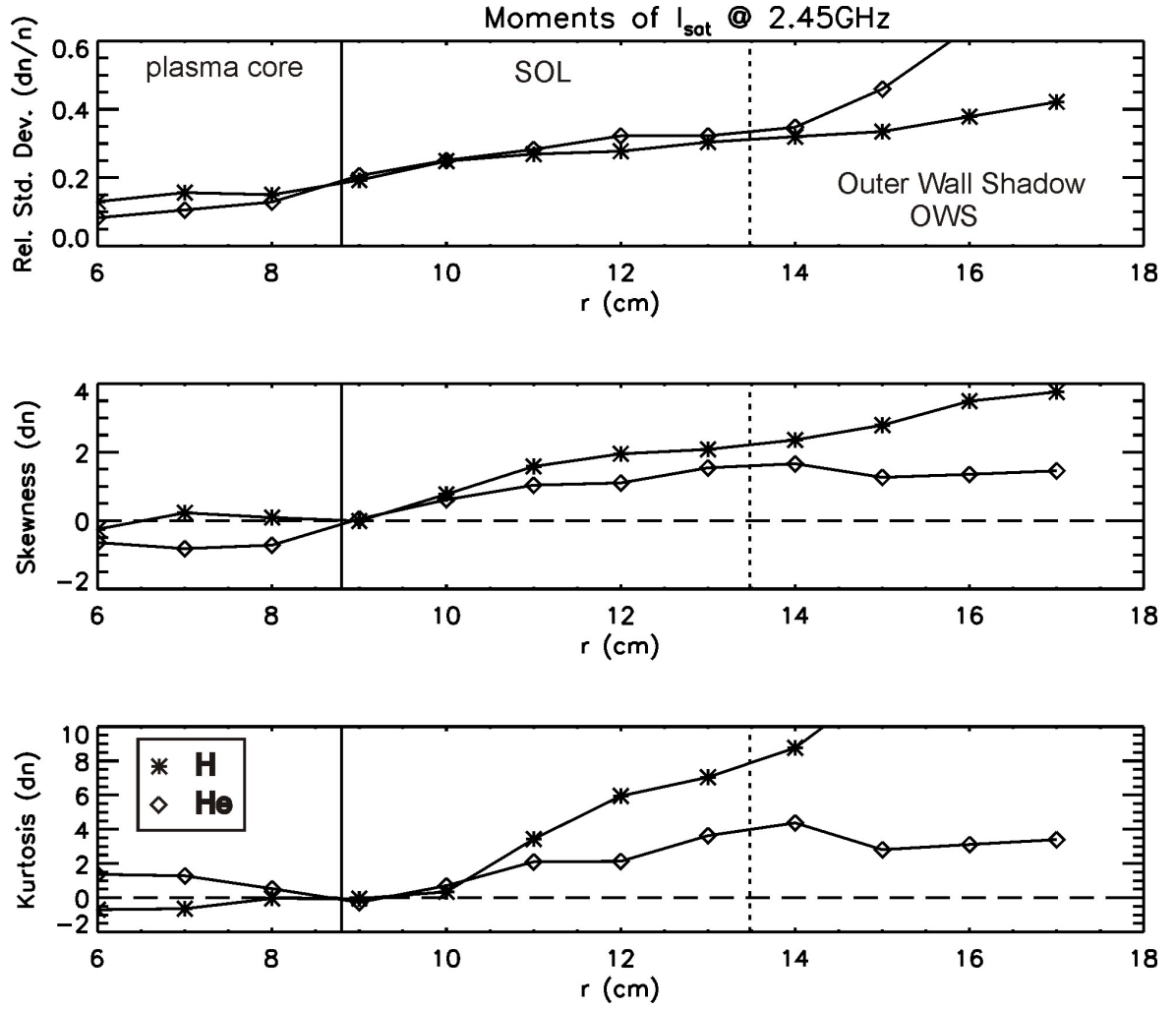
Figure 6.3: Radial profiles of the statistic moments on the ion-saturation current fluctuations in low magnetic field TJ-K discharges of hydrogen and helium.

6.2 Probability Density Functions

The shape of the probability-density function (PDF) can be characterized by the statistical moments. The relative standard deviation, skewness and kurtosis of ion-sturation current fluctuations in TJ-K discharges are presented in this section. The fluctuation data were taken in discharges #4613 (H) and #4612 (He) for the low and in discharges #4635 (H) and #4624 (He) for the high magnetic field. For the calculation of the standard deviation, they were normalized to the absolute DC values of I_{sat} from equivalent discharges (see Sec. 6.1).

Fig. 6.3 shows radial profiles of the statistical moments in hydrogen and helium discharges at low magnetic field. The relative standard deviation is shown at the top. It increases from about 10% in the plasma core to 20% at the separatrix and reaches 30% at the border between SOL and OWS. Skewness and kurtosis are zero close to the separatrix,
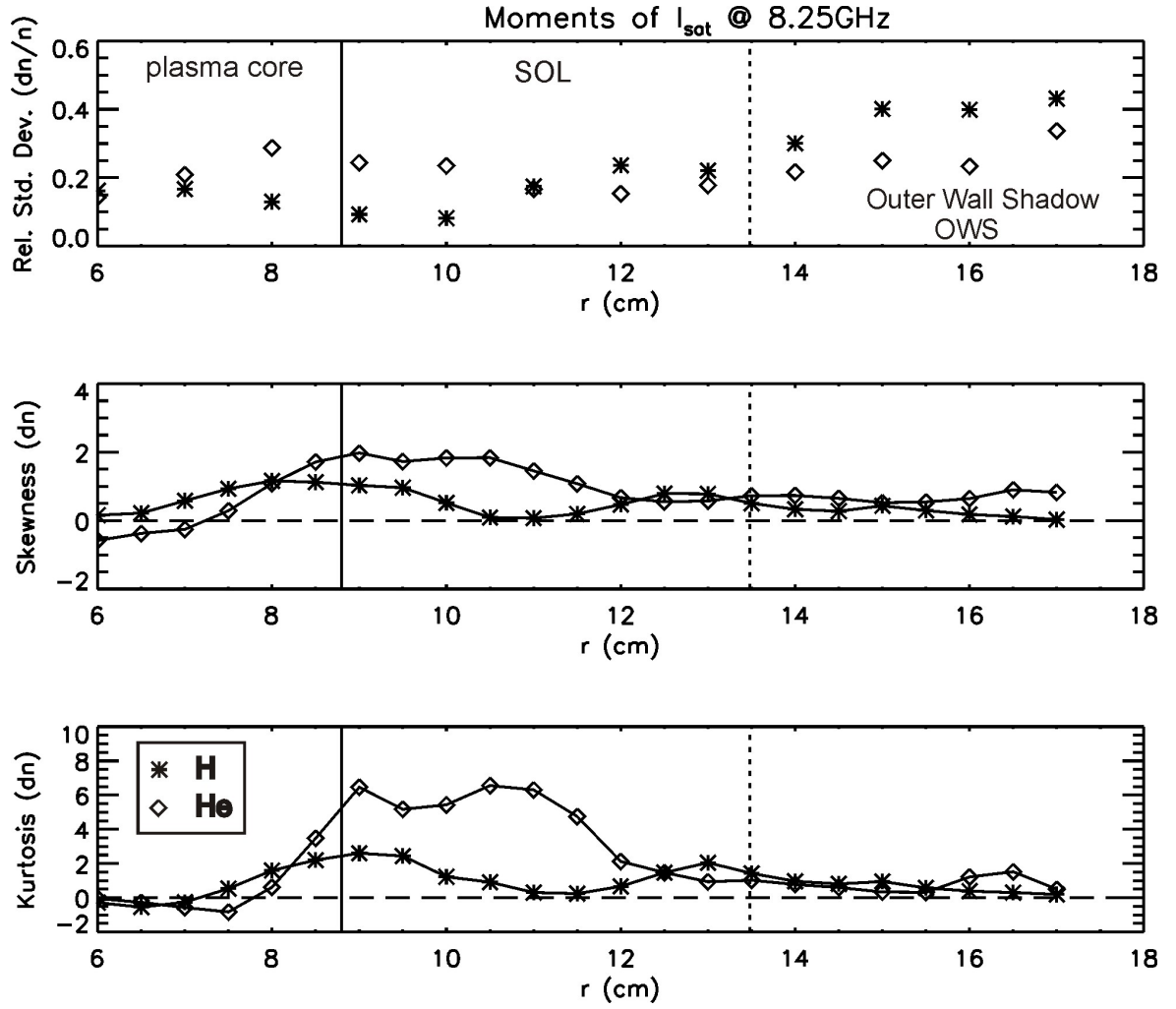
Figure 6.4: Same representation as Fig. 6.3 but with higher magnetic field.

i.e. the PDF is Gaussian there. The skewness stays between -1 and $+0.2$ in the confined plasma and increases up to $+2$ in the SOL. The kurtosis stays between -1 and $+2$ in the confined plasma and reaches $+8$ (H) and $+4$ (He) at the beginning of the OWS. This means, that the PDF transforms from a Gaussian at the separatrix to a asymmetric and sharply peaked one in the OWS. The OWS itself is of no interest since it is too far from the plasma core and has poor densities.

Fig. 6.4 gives the statistical moments of high magnetic field discharges. For $r < 14$ cm, the relative standard deviation scatters around 20% and increases for larger radii to 40%. The tendency of these curves is not as obvious as it was for the low magnetic in Fig. 6.3. This is possibly caused by normalization errors due to a drift of the plasma column as discussed in the next section. For both gases, large positiv deviations of skewness and kurtosis from zero are found. This is the case in the range $r = 7 - 10$ cm for hydrogen and in the range $r = 8 - 12$ cm for helium.

6.3 Correlation analyses

Fig. 6.5 shows characteristic parameters obtained from correlation analyses of density fluctuations at low magnetic field. The radial dependence of the auto-correlation times τ_{auto} is plotted in the upper part of the figure. Long helium auto-correlation times with values around $35\,\mu s$ were found in the plasma core. Right after the separatrix, a fast decrease is observed in the first half of the SOL. In the second half of the SOL and the following OWS the helium auto-correlation time remains constant about $15\,\mu s$. For hydrogen discharges the global behavior is similar. Compared to the helium discharge, τ_{auto} is somewhat smaller inside and larger outside the core. In the middle of Fig. 6.5 the poloidal phase velocity is shown. It is obtained from cross-correlation analyses of probe tip 4 with tips number 2 and 5. Their distance of $2\,cm$ is divided by the total time delay between these pins. The velocity is found almost constant for both gases with values of $+3\pm 1\,km/s$ in the radial range $r = 10 - 17\,cm$. Close to the separatrix, both phase velocities change their sign from positive to negative values. In the plasma core a constant downward phase velocity between -1 and $-1.5\,km/s$ is observed in the hydrogen discharge. In the helium plasma, high velocities are observed in the core plasma and close to the separatrix. This observation is probably due to structures propagating mainly perpendicular (i.e. radial) to the probe array. Such structures are picked up simultaneously with all probes leading to a large overestimation of their poloidal velocity. Therefore, the high core velocities of the helium discharge are not represented in the plot. The directions of toroidal magnetic and radial electric fields are indicated in the upper part of the plot. The electric field is known from Fig. 6.1. The resulting $E \times B$ drift is marked with vertical arrows. The electron diamagnetic drift (Eq. 2.12) is directed downward.

The estimated poloidal extent of the structures are shown in Fig. 6.5 (bottom). They were found to be $L_\theta = 55 \pm 10\,mm$ for both gases in OWS and far SOL. Close to the separatrix, the linear interpolation of two probes leads to an overestimation of the poloidal size in helium. For hydrogen discharges, L_θ was found to be $25 - 30\,mm$ in the confined plasma core.

The results of poloidal correlation analysis at high magnetic field are given in Fig. 6.6. In hydrogen discharges, auto-correlation times of $22\,\mu s$ are found in the plasma core and $16\,\mu s$ in the SOL. In-between a maximum of $\tau_{auto} = 37\,\mu s$ is observed at $r = 9\,cm$. For helium, τ_{auto} was found constant at $13 \pm 1\,\mu s$ except a maximum of $22\,\mu s$ at $r = 10 - 12\,cm$. The poloidal phase velocity is given in the middle of Fig. 6.6. It shows an abrupt change of the phase velocity direction as already seen in Fig. 6.5 for low magnetic field plasmas. In the high magnetic field hydrogen discharge, $v_\theta = -1 \pm 0.5\,km/s$ for $r < 9\,cm$ and $v_\theta = 2 \pm 0.5\,km/s$ for $r > 10\,cm$ was found. In the high magnetic field helium discharge, the values are $v_\theta = -1.5 \pm 0.5\,km/s$ for $r < 11\,cm$ and $v_\theta = 4 \pm 1\,km/s$ for $r > 12\,cm$. The radial electric field direction, as identified in similar discharges
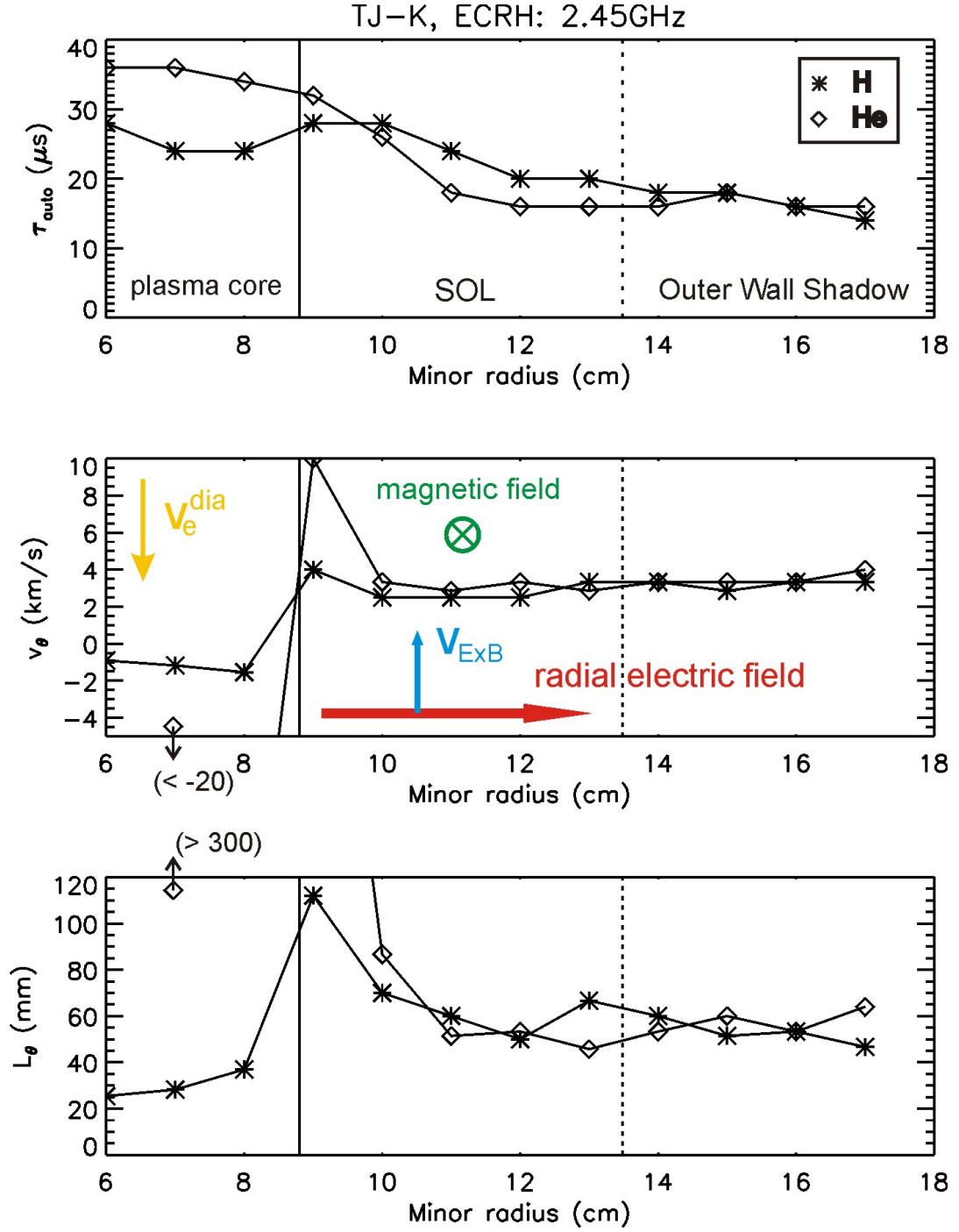
Figure 6.5: Radial dependence of auto-correlation time τ_{auto}, poloidal velocity v_θ and poloidal extent L_θ of coherent structures in TJ-K at low magnetic field. Hydrogen plasma is represented by stars and helium plasma by diamonds. Vertical lines mark the transitions from closed magnetic field lines to the homogeneous limited SOL and to the inhomogeneous outer wall shadow (OWS).
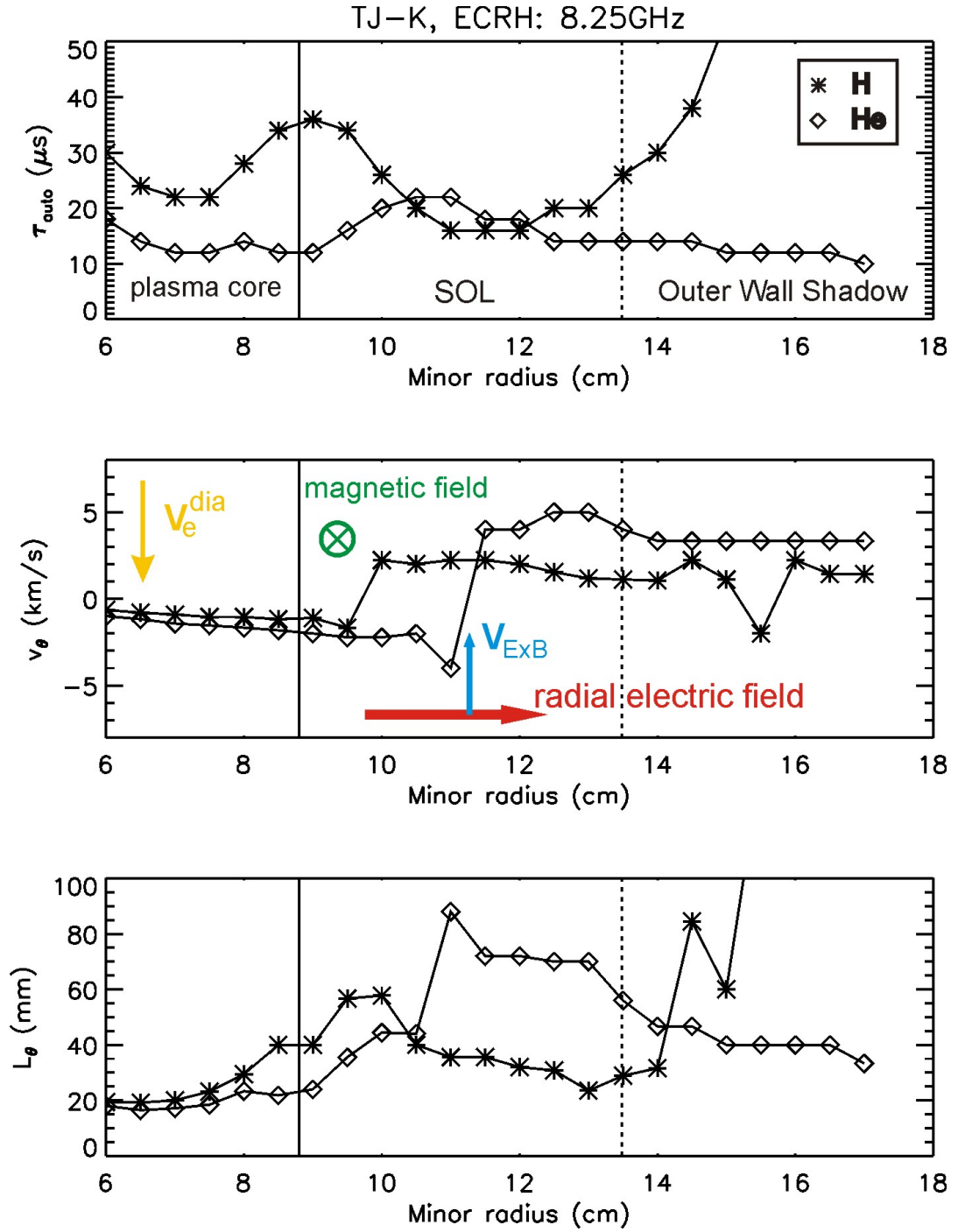
Figure 6.6: Radial dependence of correlation analyses at high magnetic field. Represented as in Fig. 6.5.

(Fig. 6.1), is indicated in the plot. The electron diamagnetic drift is directed downward. The poloidal correlation lengths estimations at high magnetic field are shown in the lower part of Fig. 6.6. In the hydrogen plasma, $L_\theta \approx 2$ cm for $r < 8$ cm, followed by a maximum of almost 6 cm in the range $r = 9 - 10$ cm. For $r > 10$ cm it is $L_\theta \approx 3$ cm. In the helium plasma $L_\theta \approx 2$ cm for $r < 9$ cm, followed by a maximum of 7 cm in the range $r = 11 - 13$ cm. For $r > 14$ cm it is $L_\theta \approx 4$ cm.

Remarkable is that there seems to be a radial shift of about two centimeters between hydrogen and helium profiles in all three plots of Fig. 6.6. Similar shifts are observed in the skewness and kurtosis maxima of the same discharges in Fig. 6.4. An inverse shift, with the helium pedestal at smaller radii than the hydrogen pedestal is seen in the density profiles in the middle of Fig. 6.1. The profiles were measured in similar plasmas but separate discharges. A uncontrolled drift has been detected of the current ratio between vertical and helical field coils at high magnetic fields. This drift leads to a drift of the plasma column. In this case, the flux surfaces would not be aligned with the limiter. This is possibly the reason for the shifts observed between radial profiles of different discharges at high magnetic field.

6.4 Discussion

The electron temperature profiles are almost constant in all discharges. The measured floating potential and ion-saturation current profiles are therefore proportional to plasma potential and density, respectively. In the plasma core, profiles do not show significant gradients. High density gradients are found close to the separatrix. In the SOL, radially outward directed electric fields are observed. At low magnetic field, the standard deviation of I_{sat} fluctuations increases monotonously from 10 % in the core to 30 % in the far SOL. Also in high magnetic field discharges, a radial increase of the standard deviation is observed. At low magnetic fields, the PDF transforms from a Gaussian at the separatrix to an asymmetric and sharply peaked one in the OWS. This change occurs due to positive intermittend events in the SOL. At the high magnetic field, a deviation from a Gaussian distribution is seen in the SOL near the separatrix.

Correlation analyses revealed an abrupt switch of the poloidal phase velocity. This strong velocity 'shear layer' is usually observed just inside the separatrix in tokamaks and stellerators [38]. In low magnetic field discharges, this shear occurs exactly at the predicted separatrix. At high magnetic field, the switch is observed distant to the predicted separatrix position. This radial shift is possibly due to a unwanted drift of the current ratio in the field coils at high magnetic field. The real separatrix in these discharges is therefore supposed to be at the position of the strong velocity shear. The poloidal propagation velocity of coherent structures changes from 1 km/s in the electron diamagnetic drift

direction in the plasma core to about 3 km/s in the ion diamagnetic drift direction in the SOL. These observations are conform to earlier findings in tokamaks and stellerators [38]. The propagation in the electron diamagnetic drift direction is typical for drift waves [39] and drift waves have been identified to drive turbulence in the core of TJ-K [40, 11]. In the SOL, interchange instabilities may become more important for turbulence [17]. These instabilities have no poloidal propagation mechanism and can only propagate with a background $E \times B$ plasma flow. The propagation is observed in the same direction but up to five times faster than the expected $E \times B$ drifts of 0.6 and 1.2 km/s for low and high magnetic field, respectively. Probably there is an additional mechanism driving coherent structures in the SOL, like turbulent electric fields.

For all discharges, the longest auto-correlation times were observed in the core close to the separatrix with a significant decrease in the SOL. The poloidal extent of the coherent structures increases from the core to the SOL with a maximum close to the supposed separatrix position. The absolute structure sizes do not fit to scalings found earlier. This might be due to the limited plasma radius and the influence of the shear layer close to the separatrix.

Chapter 7

Experimental Results from ASDEX Upgrade

At ASDEX Upgrade (AUG, see Sec. 3.2), two experimental campaigns have been carried out for SOL turbulence investigations in July and October 2007. Fluctuations were measured using the 14-pin Langmuir probe array (Sec. 3.5) mounted onto the mid-plane manipulator. This chapter presents the analyses of four probe strokes during L-mode discharges at identical parameters. The strokes took place at 1.5 and 3.0 s in the flat top of discharges number #22504 and #22505. The symbols corresponding to a particular stroke are shown in Fig. 7.1. Data presented in this chapter were registered during the probe inward motion exclusively, because in this case the pins are still cold. This corresponds to a measurement time of about 30 ms per stroke. As described in Sec. 3.2, the scrape-of-layer is divided into two regions, one where the magnetic field lines end in the divertor (DSOL) and one, where they are limited by the ICRH antennae limiters (LSOL). The field lines connected to the upper x-point are not seen by the probe (see Fig. 3.4). The measurement positions were mapped along the magnetic field lines onto the radial position in the horizontal plane containing the magnetic axis. Only the in the plasma midplane. The nominal separatrix position as given by magnetic reconstruction and the supposed separatrix as suggested by measurements are both indicated in this chapter. The first section of this chapter shows the equilibrium profiles, section 7.2 gives the radial dependence of the statistical moments of the fluctuations. In section 7.3 and 7.4 correlation analyses and radial transport investigations are reported. Section 7.5
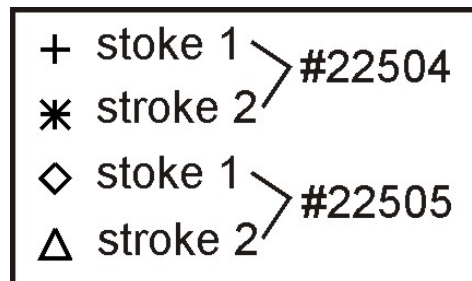

Figure 7.1: The four symbols correspond to specific probe strokes performed in the AUG discharges #22504 and #22505.
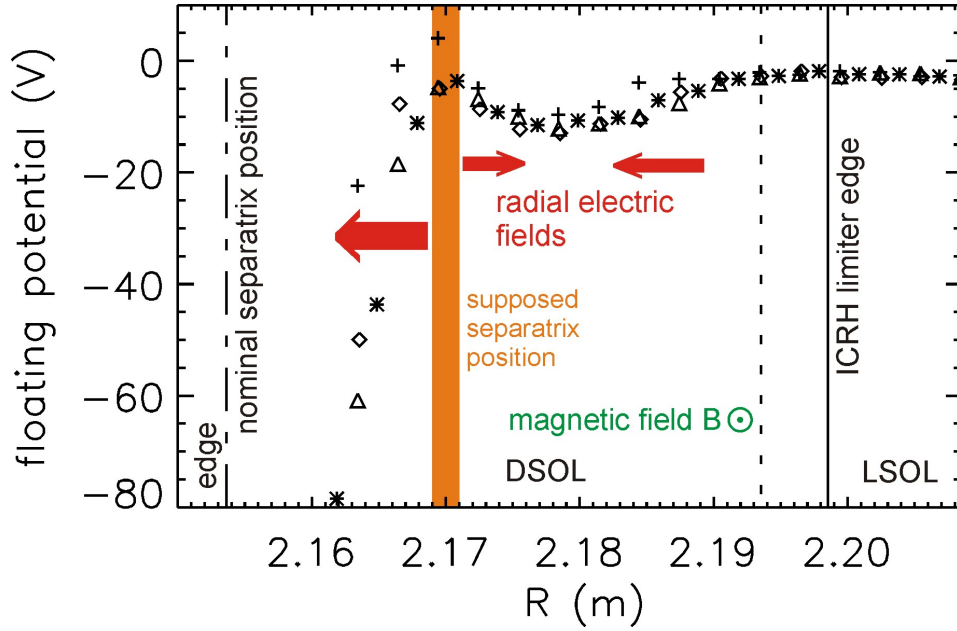
Figure 7.2: Floating potential profile in the SOL of ASDEX Upgrade during Ohmic discharges.

concludes the results obtained from AUG.

7.1 Plasma Parameters in the SOL

This section presents the equilibrium profiles measured in AUG. In Fig. 7.2, the mean floating potential is plotted for two strokes in each of the discharges (#22504 and #22505). The confined plasma region ends at the nominal separatrix at $R = 2.154$ m. Due to the strong heat load of the probes, up to this position no measurements could be carried out. Throughout the LSOL and entering one centimeter into the DSOL a constant negative potential of about -3 V is observed. At $R = 2.178$ m, the potential shows a local minimum with a value of about -12 V. This is followed by a maximum of up to $+5$ V around $R = 2.17$ m. For smaller radii the potential drops dramatically to values of -80 V and lower. In a constant temperature profile, these floating potential variations would cause radial electric fields of -110 V/cm in the range of $R = 2.16 - 2.17$ m, about $+12$ V/cm for $R = 2.17 - 2.18$ m and about -6 V/cm for $R = 2.18 - 2.19$ m.

Fig. 7.3 shows the mean ion-saturation current (I_{sat}) profile. A continuous increase is observed from the LSOL to a certain point in the DSOL, where a maximum is reached. Then the measured signal suddenly drops. This is due to strongly negative floating potentials in this region that approach the applied bias voltage. In this case the pins capture electrons from the plasma and the measured current decreases. Therefore, the I_{sat} signal in the gray shaded area does not represent the density any more. It is not clear
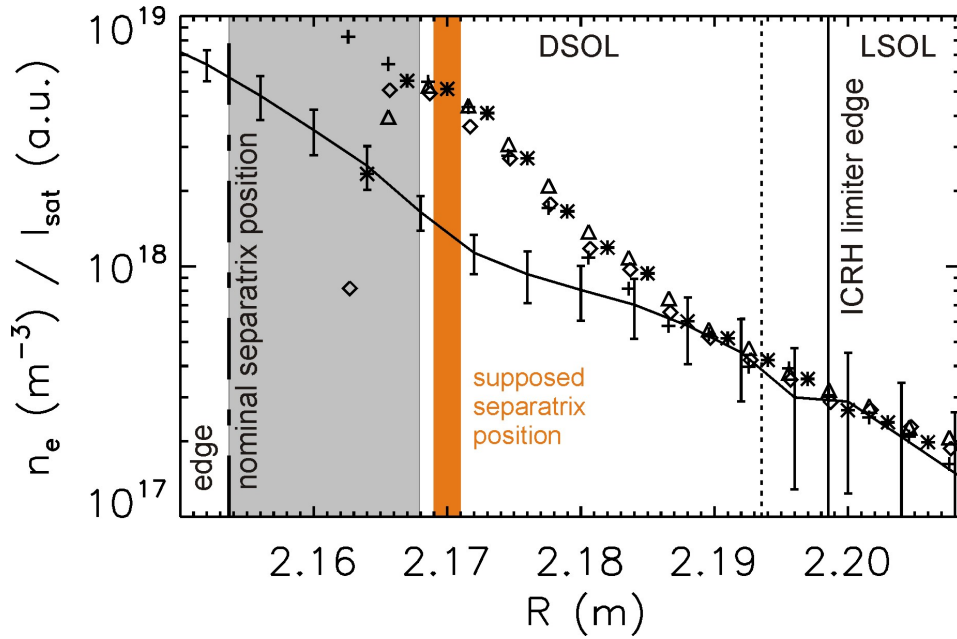
Figure 7.3: Profile of the ion-saturation current in the same representation as the floating potential in Fig. 7.2. The gray background marks the area close to the separatrix, where the measured current is no longer the ion-saturation current. The continuous line shows the electron density profile based on the lithium beam diagnostic.

why the current kept growing during the first stroke (plus signs). Although the signals in the gray shaded region are not expected to contain reliable information on absolute density values, they might still reflect the statistical properties and phase information of density fluctuations. Therefore, these signals are included in the following analyses, but they have to be treated with caution.

A swept Langmuir probe did not work properly and the Thomson scattering system measured the electron temperature in the plasma core. For these reasons, no electron temperature profiles are available. T_e is generally found around $10\,\text{eV}$ in the SOL of similar discharges at AUG. The ion temperature T_i is shown in Fig. 7.4. Based on I_{sat} and density profile, it was estimated using equation 3.3.

7.2 Probability Density Functions

In this section, the radial dependence of the I_{sat} probability density function (PDF) in the SOL of ASDEX Upgrade is discussed. For this purpose, radial profiles of the statistical moments are shown in Fig. 7.5. The upper part shows the standard deviation as a function of distance d to the nominal separatrix position. In each of the four probe strokes, the relative standard deviation was found to decrease slowly from above $50\,\%$ in the far LSOL to $40\,\%$ in a distance of $30\,\text{mm}$ to the separatrix. From this point, the
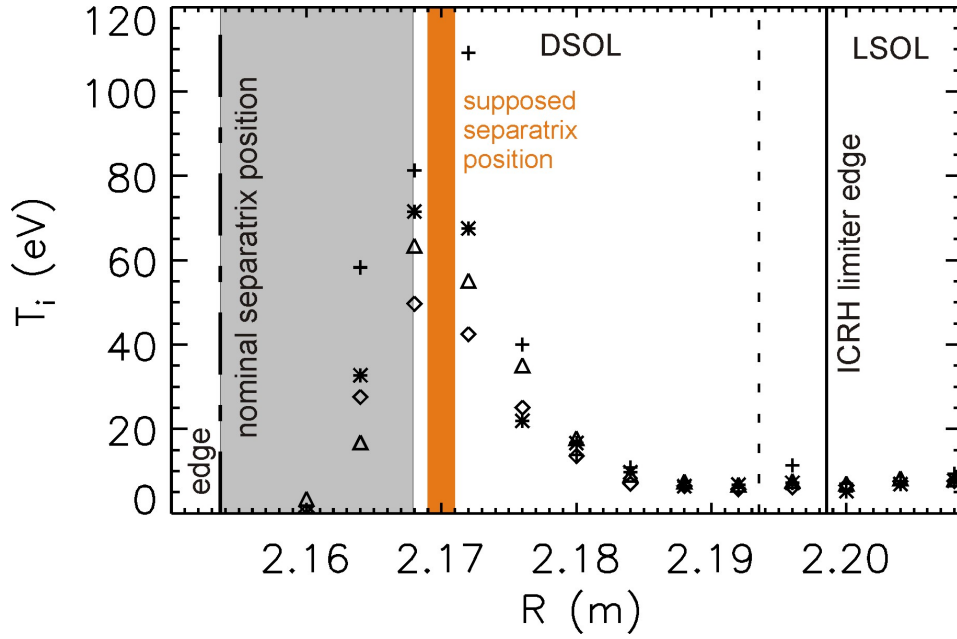
Figure 7.4: Profile of the ion temperature in the SOL of AUG approximated using equation 3.3 in the same representation as Fig. 7.2.

deviation decreases faster but still linear until a minimum at $d = 13\,$mm is reached. The steep increase closer to the nominal separatrix position is not represented in the plot because the values exceed 100% after a few milimeters in the gray shaded region. In this area the probes start to collect electrons. The strong decrease of the mean values seen in Fig. 7.3 at $R < 2.165\,$m is the reason for this increase of the relative standard deviation. Hence, this data does not provide reliable information on the relative density fluctuations for $d \leq 10\,$mm.

In the middle of Fig. 7.5 the corresponding values of the skewness are shown. They increase in the DSOL from $S \approx 0$ at $d = 15\,$mm to $S \approx 1$ at $d = 30\,$mm. For $d \geq 30\,$mm, the skewness is almost constant. This indicates that in the far-DSOL and LSOL, large positive (=high density) perturbations are more frequent than large negative ones. The fact, that the value stays constant could be a hint, that these structures appear at $d \approx 12\,$mm and then propagate radially outward. In the gray shaded area, no clear tendency of the skewness could be identified because negative and positive values are observed with the same statistics. For reliable information from this region, longer time traces with higher bias voltage would be necessary.

Kurtosis values are shown at the bottom. In the range $d = 13 - 30\,$mm, the values of the kurtosis from the four strokes follow a common curve. This curve leads from a constant level close to zero between $d = 13 - 24\,$mm, to a level of $K \approx 2$ at $d = 30\,$mm. For $d > 30\,$mm the kurtosis scatters between 0.5 and 6.5. Reproducibility of these values could probably be increased if longer time series were available. For $d < 10\,$mm a steep increase of the kurtosis values is observed that exceeds ten and is not represented in the
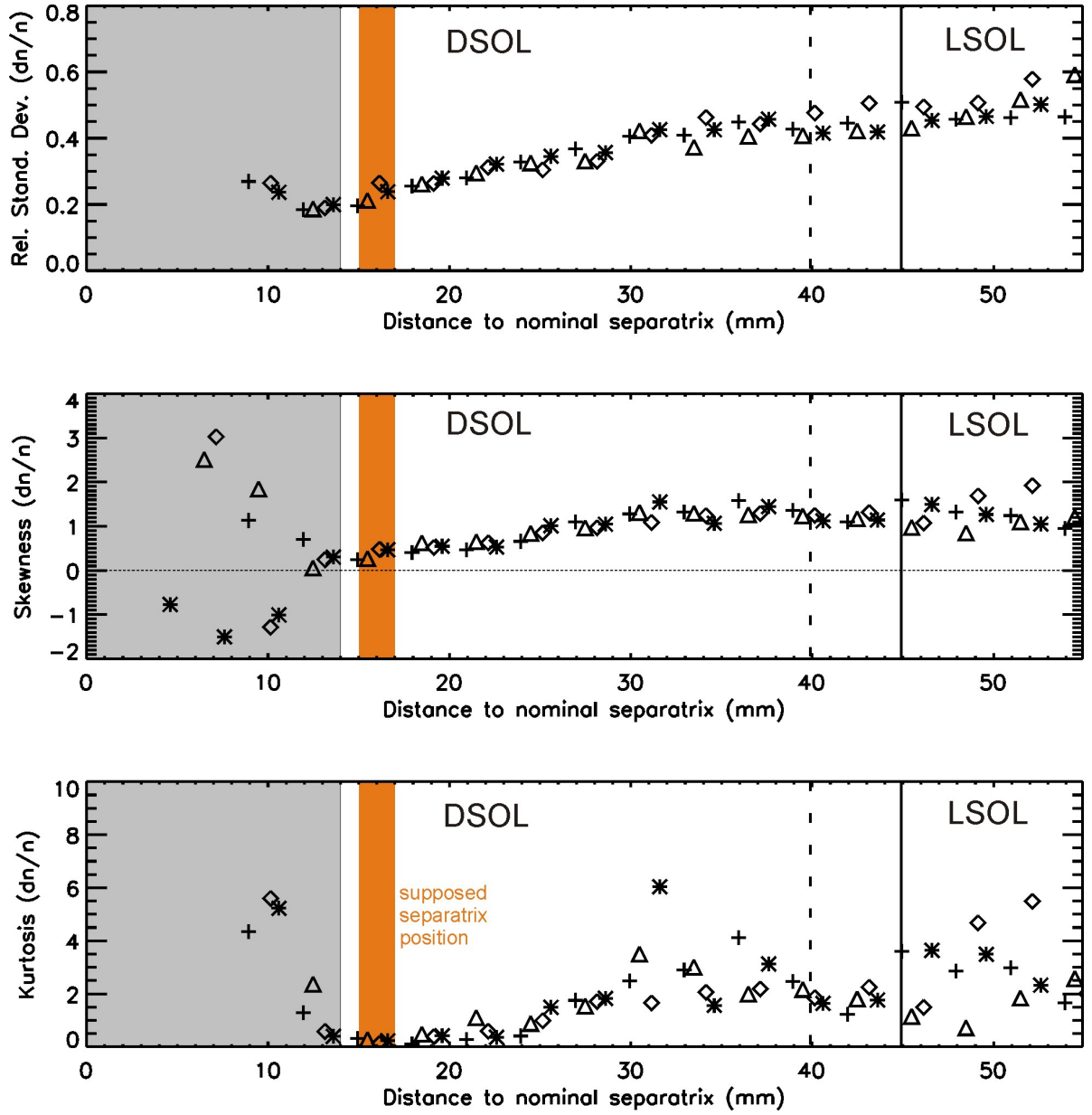
Figure 7.5: Radial dependence of ion-saturation current fluctuations in the SOL of ASDEX Upgrade. Standard deviation, skewness and kurtosis of the fluctuations plotted as a function of the distance to the nominal separatrix position.

plot.

In summary, the PDF becomes more and more Gaussian, approaching the separatrix from $d = 30$ to $d = 13\,mm$. Closer than $13\,mm$ to the nominal separatrix position it was not possible to characterize the shape of the PDF because signals might be perturbed and too short for stable statistics. The PDF is almost constant in the far DSOL and LSOL, where the plasma density is low. This range is characterized by positive high density events. This behavior is called intermittent and often observed in magnetically confined plasmas [41].

7.3 Correlation Analyses

Here, the results of correlation analyses are presented, as introduced in section 5.3. They are based on I_{sat} measurements with the poloidal 14-pin probe array in the SOL of ASDEX Upgrade. Fig. 7.6 shows the dependence of the auto-correlation time τ_{auto} from probe number 5 (see Fig. 3.7) as function of the distance to the nominal separatrix position. These values represent the characteristic time, a turbulent structure needs to pass the probe pin. Given that the lifetime of the structure is longer than the correlation time, τ_{auto} depends on the characteristic size given by L_θ and L_r and the propagation velocities in poloidal and radial direction, v_θ and v_r, respectively. In the LSOL and far DSOL, a wide scatter of the auto-correlation times was observed with a lower limit of about $20\,\mu s$. For $d \leq 30\,mm$, short correlation times of $\tau_{auto} \leq 10\,\mu s$ are found. This value decreases to $2\,\mu s$ at $d = 24\,mm$ and stays constant down to $d = 18\,mm$ where it increases stepwise up to $6\,\mu s$. For $d < 18\,mm$ no further changes are observed.

The poloidal propagation velocity v_θ of the correlated structures is shown in the middle of Fig. 7.6. The values are obtained from cross-correlation between probe pins number 4 and 7 (see Fig. 3.7). A slow downward flow of the structures with a velocity below $1\,km/s$ is observed in LSOL and far-DSOL. The downward speed increases to a value of -5 to $-8\,km/s$ from $d = 29$ to $21\,mm$. At smaller radii, the only difference between the two discharges comes up: The maximum speed is $-7\,km/s$ in both strokes of discharge #22504 and $-4.5\,km/s$ for the strokes of discharge #22505. It is not clear what could be the reason for this difference. These values remain constant down to $d = 16\,mm$. At this position all observed poloidal velocities abruptly change sign and reach the common value of $+2.5\,km/s$, which stays nearly constant for smaller radii. The direction of the magnetic field and the radial electric fields identified in the floating potential profile (Fig. 7.2) are indicated in the plot. The direction of the resulting $E \times B$-drifts are indicated by vertical arrows. It can be seen that the phase velocity roughly follows the $E \times B$ flow, leading to strong flow shear at $d = 15\,mm$. Quantitative analyses of the plasma potential could not be performed because of the missing electron temperature
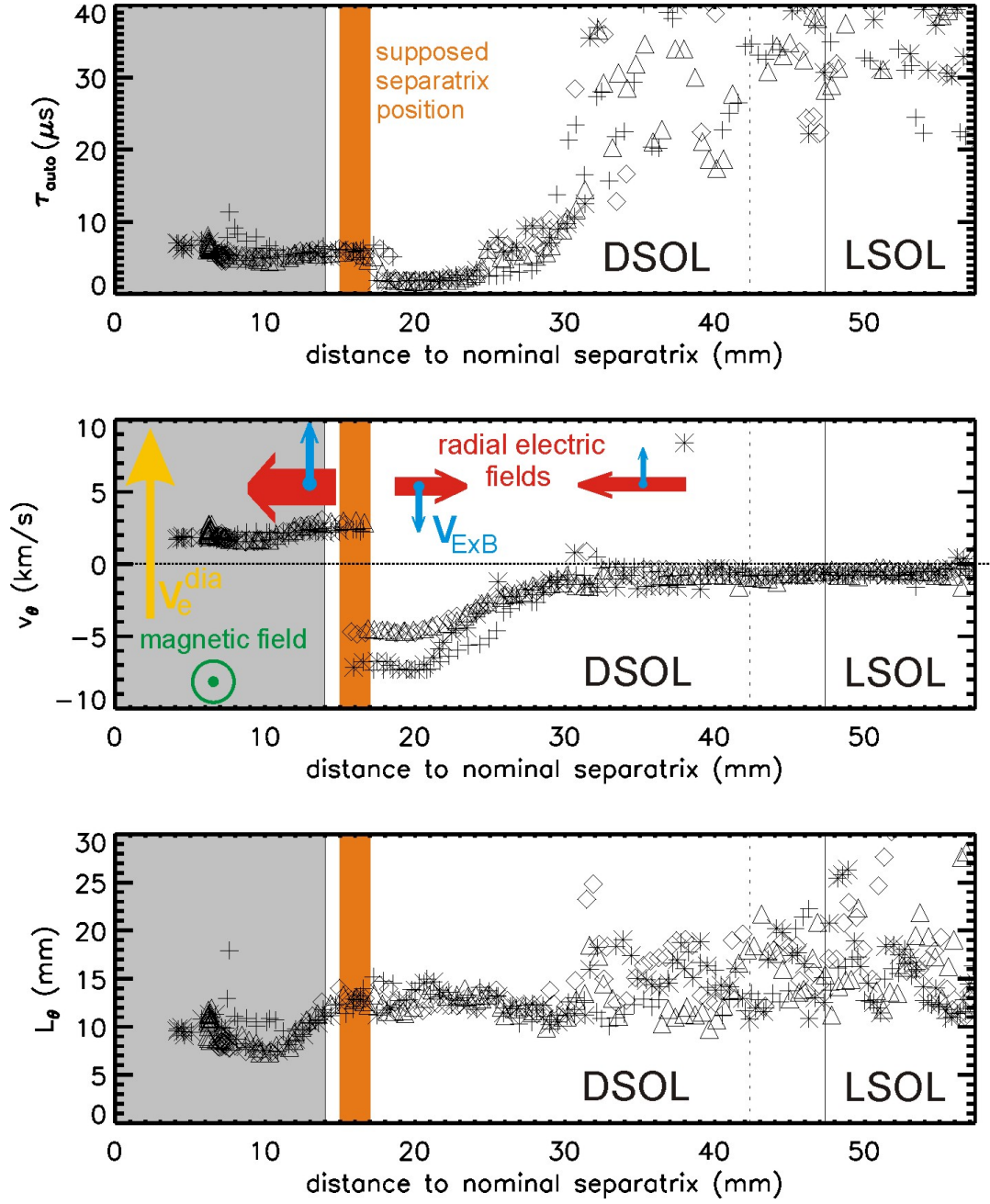
Figure 7.6: Radial dependence of auto-correlation time τ_{auto}, poloidal velocity v_θ and poloidal correlation lenth L_θ as obtained from I_{sat} correlation analyses.

profiles. Large T_e gradients, as usually observed close to the separatrix could change the here used floating potential profiles.

At the bottom of Fig. 7.6, the poloidal correlation length L_θ of the structures are estimated by interpolation of probe pins number 4 and 7. From LSOL to the far-DSOL, L_θ is found to scatter between $L_\theta = 10$ and $25\,\text{mm}$. For $d = 15 - 30\,\text{mm}$, the values of L_θ from the 4 strokes are consistently in the range $L_\theta = 10 - 15\,\text{mm}$. For $d = 11 - 15\,\text{mm}$, a decrease to $L_\theta = 7.5\,\text{mm}$ is observed. It has to be stressed, that the decrease in L_θ occurs not in the region of strong flow shear but $\approx 1\,\text{cm}$ inside of it.

In summary all results from correlation analyses showed significant changes close to a shear layer, which has been observed in the poloidal phase velocity at $d = 16\,\text{mm}$. τ_{auto} decreases significant at $d = 17\,\text{mm}$, because of the increasing absolute phase velocity. The floating potential profile reaches its maximum at the same position. L_θ increases a few millimeters before the shear layer is reached and the PDF is almost Gaussian distributed. All these findings indicate a prominent position in the plasma at $d = 16\,\text{mm}$. Earlier investigations identified similar shear layers [38], similar radial electric fields [23] and similar PDFs [42] at the separatrix. For these reasons, the distance $d = 16\,\text{mm}$ to the nominal separatrix is in the following named supposed separatrix position.

7.4 Radial Transport

In this section, the average cross-phases and radial transport are investigated. The phase relation between density and poloidal electric field fluctuations determines the sign of radial transport (Sec. 2.3).

For this evaluation, the density is approximated by the ion-saturation current and the poloidal electric field by two poloidally separated floating potential measurements. Fig. 7.7 shows the radial dependence of the average cross-phase calculated according to equation 5.10. With regard to transport, a phase lower than $\pi/2$ represents positive, i.e. net outward transport. For AUG, a value of $\varphi_{nE} \approx \pi/2$ is found in the entire radial range. This value is characteristic for drift waves and points to the drift wave as a dominant instability in the SOL of AUG. Their propagation in the electron diamagnetic drift direction might be superimposed by the poloidal $E \times B$ background flow. Furthermore it is mostly $\varphi_{nE} < \pi/2$, which indicates net outward transport. Only in the range $d = 14 - 18\,\text{mm}$, cross-phases above $\pi/2$ are observed. This suggests local inward transport. A comparison with the absolute transport levels in the SOL support this finding (Fig. 7.8). In the range of $d = 13 - 17\,\text{mm}$ net radial inward transport is observed. This seems surprising and will be verified in future measurements. A plasma source would be necessary at $d = 17\,\text{mm}$ to maintain such a net transport profile. This might occur,
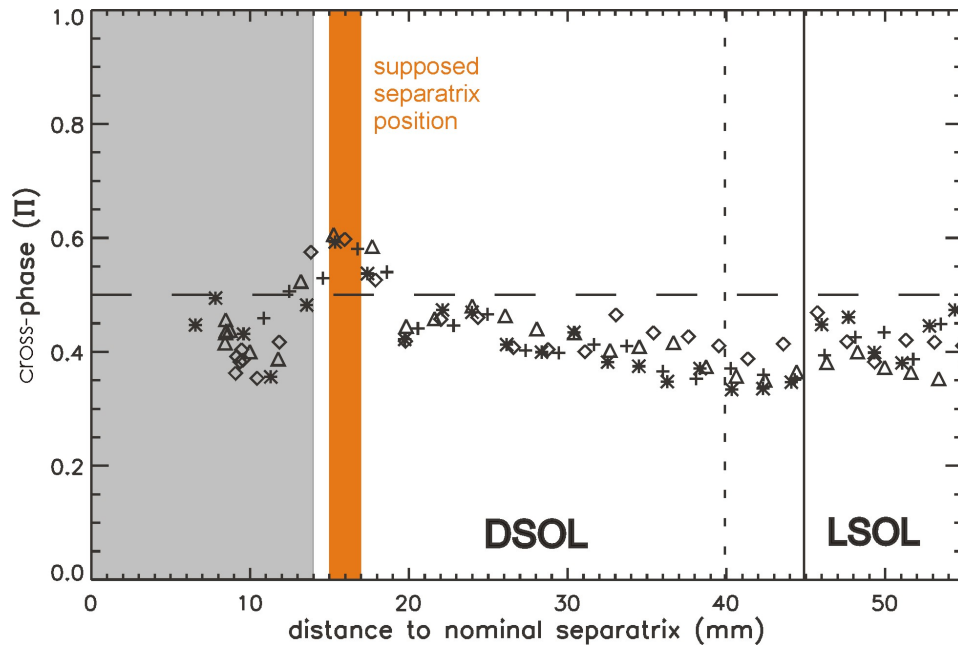
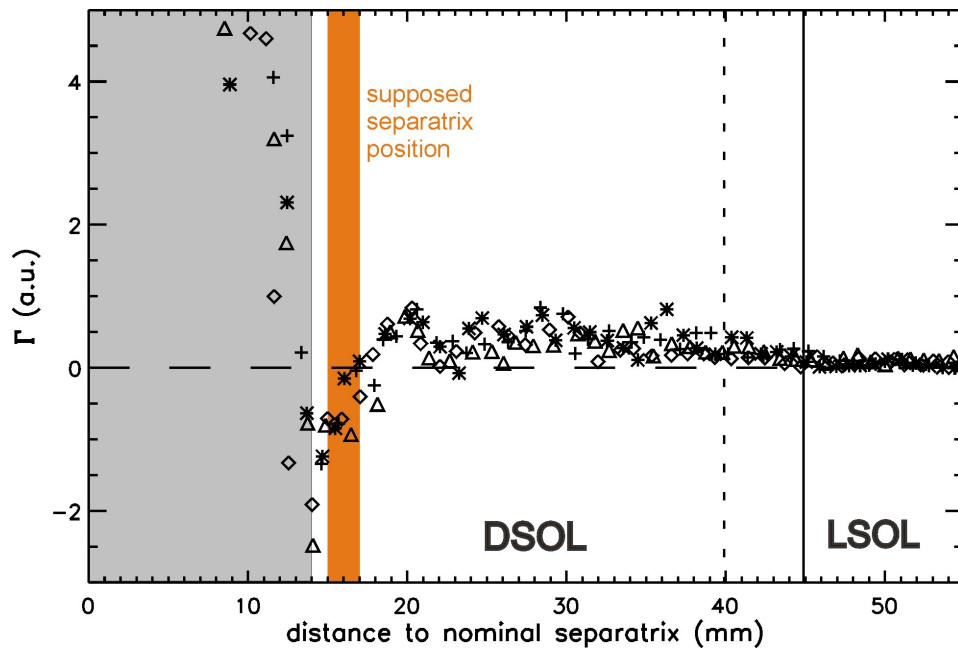**Figure 7.7:** Average cross phase between density and poloidal field fluctuations.

Figure 7.8: Profile of the radial turbulent transport.

when neutral gas from the wall is ionized close to the separatrix. An other reason could be a poloidal dependence of the radial transport, as seen earlier in other tokamaks [38]. In this case, local areas of inward transport could be compensated by poloidal and/or parallel transport from regions with net outward transport.

On the other hand, the exact position of the probe pins has to be taken into consideration. Pins number 1 and 3 (Fig. 3.7) measure the floating potential. Their distance to the separatrix differs by 1 mm. They capture therefore not only the poloidal, but also a radial component of the electric field. In the range of strong radial electric field gradients, this might influence the measurement of $\tilde{E}_\theta$.

7.5 Discussion

The poloidal phase velocity was found to change from $+2.5$ km/s to about -6 km/s at the distance $d = 16$ mm from the nominal separatrix position. This abrupt change from the electron-diamagnetic-drift direction to the ion-diamagnetic-drift direction has also been observed at the separatrix of other plasma devices [38]. This finding, as well as the floating potential profiles and the statistical moments, indicate that the separatrix of the presented discharges was located rather in the range $R = 2.167 - 2.172$ m, than at the reconstructed nominal position of $R = 2.154$ m. The equilibrium reconstruction of the magnetic field is usually thought to be more precise than 1 cm. The precision of the mid-plane manipulators position is in the range of a few millimeters. Presently, it is not clear how the difference between nominal separatrix position and location of the shear layer of more than one centimeter can be explained. Due to the increased absolute phase velocity, the autocorrelation time drops close to the supposed separatrix from 6 to 2 μs and increases again for $d > 24$ mm. The poloidal extent of correlated structures was found to increase from 7 mm ($d = 10$ mm) to 13 mm at the supposed separatrix. In the SOL, it is constant between 10 and 15 mm with large scatter for $d > 30$ mm. A decrease of the poloidal correlation length close to the shear layer was not observed.

The measured floating potential profiles suggest radial electric fields between -11000 and $+1200$ V/m, if the electron temperature gradient is neglected. The shape is in good agreement with recent findings obtained by doppler reflectometry at ASDEX Upgrade. Fig. 7.9 gives the radial electric fields obtained in an Ohmic discharge [43]. At the separatrix ($\rho = 1$), it shows a strong inward directed electric field. Similar fields can obtained from the floating potential in Fig. 7.2. A quantitative comparison of these fields and an estimation of the poloidal $E \times B$ drifts could not be performed because no reliable temperature profiles were available to calculate the plasma potential.

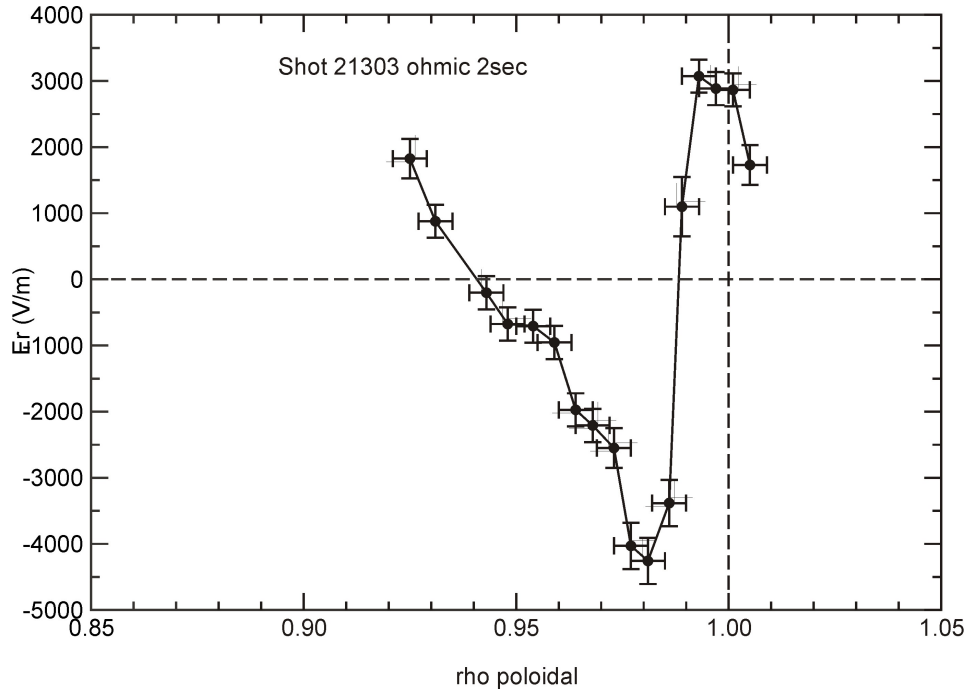The density profiles deduced from ion-saturation current measurements exceed the elec-

Figure 7.9: Radial electric fields E_r, obtained by Doppler reflectometry close to the separatrix ($\rho_{pol} = 1$) of AUG [43]. $0.01\,\rho_{pol}$ corresponds to about 5 mm.

tron density from the lithium beam diagnostic for radii $R < 2.185$ m (Fig. 7.3). This is probably due to the increasing ion temperature, which leads to an increasing ion current and therefore to an overestimation of the plasma density. The ion temperatures leading to the observed difference are shown in Fig. 7.4 and fit to temperatures obtained from lithium beam measurements.

The investigation of the statistical properties brought up the following results. The standard deviation of the ion saturation current increases from 20 % at the supposed separatrix to more than 40 % in the far-DSOL. This is consistent with findings in the DIII-D tokamak [44]. Skewness and kurtosis suggest the transformation from a Gaussian PDF ($S = K = 0$) at $d = 13$ mm to a asymmetric peaked PDF ($S = 1, K = 2$) in the far-DSOL. Earlier investigations on many fusion devices showed similar intermittent events [38, 41, 42] in the SOL. Inside the supposed separatrix, which would correspond to the plasma edge, different strokes yielded different results for the skewness. One stroke is consistent with observations from DIII-D [45] and LAPD [46], where negative values of the skewness have been observed. The other strokes revealed in the confined plasma of AUG more positve skewness values than for example in the TEXTOR tokamak [47] or the linear device PISCES [42]. Longer time traces need to be analyzed to resolve the PDF in the confined plasma of AUG. This topic is part of ongoing investigations.

The average cross-phase between density and poloidal electric field was found mainly around 0.4π. In the range $d = 14 - 18$ mm, phases larger than $\pi/2$ are observed with

a maxium of almost 0.6π at the supposed separatrix. Cross-phases close to $\pi/2$ are predicted for drift-wave turbulence. Close to the separatrix, the cross-phases above $\pi/2$ are a sign of local inward transport. This might be related to the shear in the poloidal $E \times B$ velocity (Fig. 7.2). Analytical studies have shown that strong shear can lead to cross-phase modifications toward local inward transport [48]. In the present case, the inward transport might also be due to correlations of density and spurious poloidal velocity fluctuations. For more detailed analyses of the turbulent transport, probe arrays with the tips aligned to the flux surface are suggested to eliminate a possible influence of radial fluctuations. In addition, longer time traces are necessary for better statistics concerning spectral components of the transport.

All fluctuation signals from AUG proved a good reproducibility of the results. The evaluation of radial dependencies gave evidence that the separatrix was indeed located at the supposed separatrix position $R = 2.17\,\mathrm{m}$ ($d = 16\,\mathrm{mm}$).

Chapter 8
Summary and Conclusions

The understanding of plasma turbulence is object of basic research and crucial for the development of future nuclear fusion power plants. This work presents plasma investigations in the different magnetic confinement concepts realized in the torsatron TJ-K and the tokamak ASDEX Upgrade (AUG). Poloidal Langmuir probe arrays have been built for the low-temperature plasmas in TJ-K and the hot fusion plasma edge in AUG. Experiments were carried out in limited hydrogen and helium discharges on TJ-K and Ohmic discharges of deuterium on AUG. Plasma profiles and fluctuations have been measured in the scrape-off layer (SOL) and the confined plasma of both devices. Different analysis techniques have been applied to the data and the results were discussed in relation to theoretical models and other experimental findings.

The density decay length has been determined in both devices, to compare their non-dimensional plasma parameters. The results confirmed the dimensional similarity between TJ-K and ASDEX Upgrade discharges.

Cross-correlation analyses revealed an abrupt change in the poloidal phase velocity in all discharges at TJ-K and AUG. This change is supposed to mark the transition from closed field lines to the SOL and has also been observed in other devices [38]. This position is called separatrix in the following, although it was not always observed exactly at the nominal separatrix position. In the plasma core, the phase velocity points into the electron-diamagnetic drift direction. Drift waves are expected to propagate in this direction, if no poloidal background flow is present. The floating potential profile of AUG indicates radial electric fields similar to those found by Doppler reflectometry [49]. This causes a poloidal $E \times B$ drift and leads to a shear layer in the poloidal background flow. Quantitative $E \times B$ flow velocities cannot be given because the electron temperatures are not known with sufficient accuracy to calculate the plasma potential. But the abrupt shift seems to arise rather from the background shear flow, than due to a change in the turbulence mechanism. Otherwise a more continuous change would be expected. The measured cross-phase $\varphi_{nE} = \pi/2$ indicates drift wave turbulence in both, confined plasma and SOL. The presence of drift waves in the TJ-K plasma has already been shown

by earlier investigations [40, 11]. This is probably also the reason for the observed phase velocity just inside the separatrix. In contrast to AUG, no strong radial electric field has been identified in the confined plasma of TJ-K. The propagation in TJ-K is therefore not due to a poloidal $E \times B$ background flow.

The poloidal correlation length L_θ increases in both experiments just inside the separatrix by a factor of two. The increased level remains almost constant in the SOL. This indicates that the edge turbulence is modified before the velocity changes abruptly at the separatrix. The increase of L_θ close to the separatrix is not yet understood. Common turbulence models predict radial decorrelation due to the shear layer. This is not implicitly in contradiction to the increasing L_θ, because the correlated structures might be strongly elongated in the poloidal direction. Recent biasing experiments in TJ-K revealed larger correlation length in presence of a shear layer [50]. The increasing L_θ leads also to longer auto-correlation times τ_{auto}, although this influence is partly compensated by a slight increase of the phase velocity. Larger structures can be observed during a shorter time, if they propagate faster. At the separatrix, the absolute value of the phase velocity doubles, while the poloidal correlation length stays constant. This is the reason for the decrease of the auto-correlation time just outside the separatrix. The structures move faster and are seen for a shorter time by the probes.

Close to the separatrix of AUG, indications for net inward transport were observed. This finding has to be confirmed by further investigations. In TJ-K, inward transport was found in presence of a shear layer for high frequencies [50]. The cross-check of this finding with TJ-K results is object of ongoing research. Correlation analyses with a fixed reference probe gave a 2D impression of turbulence in TJ-K. In AUG, the principle feasibility of similar experiments was shown. However, the plasma density at the reference probe was too low and the time traces were too short for useful cross-correlation analyses. The results of parallel correlation were not shown in this work.

The relative density fluctuation level is similar in both experiments. The increase of their standard deviation with radius might be due to outward propagating density events with increasing relative importance compared to the background density.

The probability density function was found asymmetrical and peaked ($S = 1$, $K = 1$) in the SOL of TJ-K and AUG. This is a clear indication for the presence of intermittent density events and has also been observed in other devices [41, 42]. At the separatrix, the PDF was found to be Gaussian ($S = 0$, $K = 0$). For this reason, it is not likely that these positive density perturbations pass the separatrix. It is more likely, that they develop close to the separatrix. Negative skewness values were observed in the confined plasma of TJ-K. For a final determination of the edge skewness in AUG, better statistics would be necessary. Negative values could be caused by density holes propagating from the separatrix to the core plasma. This mechanism has already been observed in the

linear device LAPD [46] and the tokamak DIII-D [45]. Better statistics are necessary for a final determination of the skewness in the confined plasma of AUG.

In ASDEX Upgrade, a new reference probe is currently installed on a protection limiter. This probe is suitable for future parallel correlation studies with the mid-plane manipulator. Additional fluctuation data were recorded using a high-speed camera and a high-speed channel of the lithium beam diagnostics, during the last campaign. This data is already available and should be analyzed, to involve these diagnostics in future investigations.

For future campaigns at TJ-K, a second poloidal limiter plate was constructed. It separates microwave antenna and probe array toroidally, to ensure that the probes are not connected to locally heated flux tubes of the SOL. Additionally, the available heating power for high magnetic field discharges was doubled. Together with simultaneous acquisition of fluctuation and DC background, this will further improve quality and reliability of TJ-K turbulence investigations. Such improved measurements are currently taking place at TJ-K .

In summary it can be stated, that the investigated turbulent properties were found to be quite similar in TJ-K and AUG. The dimensionally similar discharges seem to develop a similar kind of turbulence, as suggested by numerical simulations. In the plasma edge of TJ-K and probably also of AUG, drift waves seem to be the dominant instability. The driving instability in the SOL and the detailed transition processes at the separatrix are interesting questions for future investigations.

Bibliography

[1] U. Stroth, *Einführung in die Plasmaphysik* (Institut für Plasmaforschung, Universität Stuttgart, Stuttgart, 2007).

[2] U. Stroth, Plasma Phys. Controll. Fusion **40**, 9 (1998).

[3] H. Weisen et al., Nucl. Fusion **37**, 1741 (1997).

[4] J.-M. Moret et al., Phys. Rev. Lett. **79**, 2057 (1997).

[5] L. Lao et al., Nucl. Fusion **41**, 295 (2001).

[6] J. W. Connor and J. B. Taylor, Nucl. Fusion **17**, 1047 (1977).

[7] R. E. Waltz, J. DeBoo, and M. N. Rosenbluth, Phys. Rev. Lett. **65**, 2390 (1990).

[8] A. Hasegawa and M. Wakatani, Phys. Rev. Lett. **50**, 682 (1983).

[9] C. Lechte, S. Niedner, and U. Stroth, New J. Phys. **4**, 34.1 (2002).

[10] S. Niedner, B. D. Scott, and U. Stroth, Plasma Phys. Controll. Fusion **44**, 397 (2002).

[11] U. Stroth *et al.*, Phys. Plasmas **11**, 2558 (2004).

[12] M. Ramisch, *Scaling and Manipulation of Turbulent Structures in the Torsatron TJ-K*, Ph.D. thesis (Christian-Albrechts-Universität, Kiel, 2005).

[13] Häberle, *Skalierung turbulenter Strukturen im Torsatron TJ-K*, Diploma thesis (Universität Stuttgart, Stuttgart, 2007), .

[14] J. Wesson, *Tokamaks* (Clarendon Press, Oxford, 1987).

[15] E. J. Powers, Nucl. Fusion **14**, 749 (1974).

[16] T. Happel, *Influence of limiters on Plasma equilibrium and dynamics in the Torsatron TJ-K*, Diploma thesis (Christian-Albrechts-Universität, Kiel, 2005), .

[17] N. Mahdizadeh, *Investigation of three-dimensional turbulent structures in the Torsatron TJ-K*, Ph.D. thesis (Universität Stuttgart, Stuttgart, 2007).

[18] K. Rahbarnia, *Charakterisierung der elektromagnetischen Turbulenz im Torsatron TJ-K*, Ph.D. thesis (Universität Stuttgart, Stuttgart, 2007).

[19] N. Krause *et al.*, Rev. Sci. Instrum. **73**, 3474 (2002).

[20] E. Ascasibar *et al.*, *Plasma Physics and Controlled Fusion Research (Proc. 16th Int. Conf., Montreal, 1996), IAEA, Vienna* (IAEA, Vienna, 1996), p. 183.

[21] A. Herrmann and O. Gruber, Fus. Sci. Techn. **44**, 569 (2003).

[22] F. Wagner *et al.*, Phys. Rev. Lett. **49**, 1408 (1982).

[23] J. Schirmer, *Plasma turbulence studies using correlation doppler reflectometry on the ASDEX Upgrade tokamak*, Ph.D. thesis (Ludwig-Maximilians-Universität, München, 2005).

[24] A. Schmid et al., *ASDEX Upgrade Programme Workshop* (IPP, Ringberg, 2006).

[25] A. Schmid *et al.*, Rev. Sci. Instr. **78**, 1 (2007).

[26] J. Schweinzer et al., Plasma Phys. Controll. Fusion **34**, 1173 (1992).

[27] G. Matthews, Plasma Phys. Controll. Fusion **36**, 1595 (1994).

[28] K. Rypdal, V. Demidov, and S. Ratynskaia, Rev. Sci. Instr. **73**, 3409 (2002).

[29] M. Weinlich and A. Carlson, Phys. Plasmas **4**, 2151 (1997).

[30] N. Mahdizadeh *et al.*, Plasma Phys. Controll. Fusion **47**, 569 (2005).

[31] R. Lehmer, G. Gunner, and R. Conn, Rev. Sci. Instr. **66**, 523 (1995).

[32] B. Scott, Plasma Phys. Controll. Fusion **39**, 1635 (1997).

[33] N. Mahdizadeh *et al.*, Plasma Phys. Controll. Fusion **49**, 1005 (2007).

[34] L. Spitzer, in *Interscience tracts on physics and astronomy*, edited by R. E. Marshak (Interscience Publishers, Inc., New York, 1956).

[35] B. A. Carreras *et al.*, Phys. Plasmas **3**, 2664 (1996).

[36] C. Lechte, *Microscopic Structure of Plasma Turbulence in the Torsatron TJ-K*, Ph.D. thesis (Christian-Albrechts-Universität, Kiel, 2003).

[37] P. Manz, *Bestimmung der Energietransfer-Funktion im Torsatron TJ-K*, Diploma thesis (Christian-Albrechts-Universität, Kiel, 2005), .

[38] S. J. Zweben *et al.*, Plasma Phys. Controll. Fusion **49**, S1 (2007).

[39] F. F. Chen, Phys. Fluids **8**, 912 (1965).

[40] C. Lechte, J. Stöber, and U. Stroth, Phys. Plasmas **9**, 2839 (2002).

[41] G. Antar *et al.*, Phys. Plasmas **10**, 419 (2003).

[42] G. Antar, S. Krasheninnikov, P. Devynck, and R. Doerner *et al., Phys. Rev. Lett.* **87**, *(2001).*

[43] *G. D. Conway et al., Nucl. Fusion* **46**, *S799 (2006).*

[44] *R. et al., Nucl. Fusion* **45**, *1589 (2005).*

[45] *J. Boedo, D. Rudakov, and R. Colchin et al., Phys. Plasmas* **10**, *1670 (2003).*

[46] *T. A. Carter, Phys. Plasmas* **13**, *010701 (2006).*

[47] *Y. H. Xu, S. Jachmich, R. R. Weynants, and the TEXTOR team, Plasma Phys. Controll. Fusion* **47**, *1841 (2005).*

[48] *P. Terry, D. Newman, and A. Ware, Phys. Plasmas* **10**, *1066 (2003).*

[49] *J. Schirmer et al., Plasma Phys. Controll. Fusion* **49**, *1019 (2007).*

[50] *M. Ramisch et al., Plasma Phys. Controll. Fusion* **49**, *777 (2007).*

Acknowledgement

I wish to express my sincere thanks to